

CARBON NANOTUBE BASED HYBRID NANOSTRUCTURES AS
PHOTOTHERMAL ANTIMICROBIAL NANOMATERIALS

by

BETÜL ORUÇ

Submitted to Graduate School of Engineering and Natural Science

in partial fulfillment of

the requirements for the degree of

Master of Science

Sabanci University

Spring 2018

TITLE OF THE THESIS/DISSERTATION

APPROVED BY:

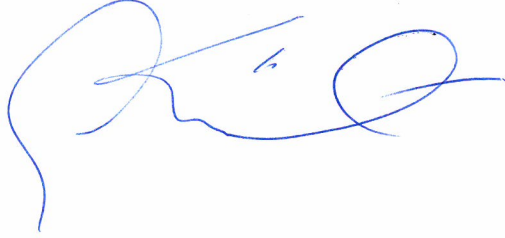
Asst. Prof. Hayriye Ünal (Thesis Supervisor)



Prof. Sedef Tunca Gedik



Prof. Kürşat Şendur



DATE OF APPROVAL: 17/07/2018

© Betül Oruç 2018

All Rights Reserved

To my loving husband

ABSTRACT

CARBON NANOTUBE BASED HYBRID NANOSTRUCTURES AS PHOTOTHERMAL ANTIMICROBIAL NANOMATERIALS

BETÜL ORUÇ

Master of Science Dissertation, July 2018

Supervisor: Asst. Prof. Hayriye Ünal

Keywords: Photothermal agents, carbon nanotubes, antimicrobial coating, antibiofilm coating, self-assembly, DNA nanostructures, fluorophores arrays

Antimicrobial resistance (AMR) is estimated to account for nearly 10 million deaths annually by 2050 according to recent high-profile reports. In this respect, AMR is a serious public health concern that requires urgent actions for combating antibiotic-resistant bacteria. Rapid progress in nanotechnology has opened new horizons for the development of innovative therapies leading to the physical destruction of bacteria as an alternative to biochemical treatments. Photothermal treatment based on nanomaterials is a remarkable solution to kill antibiotic-resistant bacteria through light induced elevated heat generation. However, their heat generation capacity is restricted to inherent light absorption properties of these nanoparticles. In this thesis, we presented two novel methods to prepare effective carbon nanotube (CNT) based photothermal agents by hybridizing with arrays of fluorophores and three-way-junctions DNA nanostructures. These hybridization methods provided an enhancement in the light absorption and heat generation capacity of CNTs and prepared nanohybrids showed remarkable photothermal activity on bacteria.

Chapter 2 describes a method to decorate the surface of multi walled carbon nanotubes (MWNTs) with an array of NIR absorbing fluorophores (3,3'-Diethylthiatricarbocyanine, DTTC) acting as a light harvesting antenna under NIR laser irradiation leading to high

temperature elevation as a result of the photothermal conversion. Continuous NIR laser irradiation of MWNT/DTTC nanohybrids for 15 minutes resulted in a local temperature of 92°C and a 77% killing efficiency on *P. aeruginosa* cells in the dispersion. In order to evaluate the photothermal activity of nanohybrids on surfaces as antimicrobial and antibiofilm coatings, MWNT/DTTC nanohybrids were incorporated into waterborne polyurethane (PU) matrix. MWNT/DTTC-PU nanocomposite generated higher temperatures reaching 120°C after only 3 minutes of laser irradiation. After multiple laser irradiation cycles, the light-activated heat generation by MWNT/DTTC-PU nanocomposite was not affected and proved their reusability potential in terms of the photothermal conversion. The antimicrobial activity of MWNT/DTTC-PU nanocomposite on surface attached *P. aeruginosa* cells was examined using confocal laser scanning microscopy.

In Chapter 3, we introduced a novel approach to improve the light absorption capacity of single walled carbon nanotubes (SWNTs) through the arrangement of three individual SWNTs into desired nanostructures with the guidance of DNA self-assembly. The specially designed DNA three-way junction (3WJ) was comprised of three Watson-Crick paired helices with non-complementary single stranded tails designed to wrap around the SWNTs surface. DNA-3WJ nanostructures acted as a dispersion agent for SWNTs and also as a rigid template for the self-assembly of SWNTs into a controlled branched nanostructure through noncovalent binding interaction at an angle of approximately 120° to each other. Hybrids of CNTs and DNA-3WJ nanostructures enabled the fluorescent labeling of SWNTs for biological and sensing applications as well. DNA-3WJ/SWNT nanohybrids presented enhanced NIR absorption and enhanced photothermal conversion with respect to individual SWNTs at the same concentration. This improvement provided a valuable approach for utilization of CNT based nanomaterials as photothermal agents with stronger photothermal activity.

Chapter 4 describes the preparation and characterization of broadband light-harvesting nanohybrids as solar photothermal agents by a self-assembly of visible light absorbing fluorophores on the CNTs surface as a continuation of Chapter 2. For this purpose, the surface of CNTs were decorated with multiple fluorophores which possess strong light absorption capacity in UV, Vis and NIR regions of the spectrum. Prepared CNT/Fluorophores nanohybrids were exposed to artificial solar light obtained by the solar simulator to investigate their photothermal conversion efficiency.

ÖZET

KARBON NANOTÜP TABANLI HİBRİT NANOYAPILARIN FOTOTERMAL ANTİMİKROBİYAL NANOMALZEMELER OLARAK KULLANIMI

BETÜL ORUÇ

Yüksek Lisans Tezi, Temmuz 2018

Tez Danışmanı: Dr. Öğr. Üyesi Hayriye Ünal

Anahtar kelimeler: Fototermal ajanlar, karbon nanotüpler, antimikrobiyal kaplama, antibiyofilm kaplama, öztoplanma, DNA nanoyapıları, florofor dizileri

Son dönemdeki yüksek profilli raporlara göre, antimikrobiyal direncinin 2050 yılına kadar yıllık yaklaşık 10 milyon insanın ölümünden sorumlu olması beklenmektedir. Bu bakımdan, antibiyotik direnci antibiyotiğe dirençli bakterilerle mücadelede acil eylem gerektiren ciddi bir halk sağlığı sorunudur. Nanoteknolojideki hızlı ilerleme biyokimyasal tedavilere alternatif olarak bakterilerin fiziksel tahribatına yol açan yenilikçi terapilerin geliştirilmesi için yeni ufuklar açmıştır. Nanomalzeme tabanlı fototermal tedavi, ışık kaynaklı yüksek ısı üretimi yoluyla antibiyotiğe dirençli bakterileri öldürmek için dikkate değer bir çözümdür. Bununla birlikte, bu nanomalzemelerin ısı üretim kapasitesi, kendinde var olan ışık emme özellikleri ile sınırlıdır. Bu tez çalışmasında, florofor dizileri ve üç kollu bağlantıya sahip DNA nanoyapıları ile hibridize edilerek etkili karbon nanotüp (CNT) bazlı fototermal ajanların hazırlanması için iki yeni yöntem sunulmuştur. Bu hibridizasyon yöntemleri, CNT'lerin ışık absorpsiyonu ve ısı üretim kapasitesinde artış sağlamış ve hazırlanan nanohidritler, bakteriler üzerinde belirgin bir fototermal aktivite göstermiştir.

İkinci bölümde yakın kızılötesi (NIR) lazer ışınımı altında anten görevi görerek NIR ışığı absorbe eden florofor dizilerinin (3,3'-Dietiltiyotiarenkosiyenin, DTTC) çok duvarlı karbon nanotüplerin (MWNT) yüzeyine dekore edilmesiyle fototermal dönüşüm

sonucunda yüksek sıcaklık artışına sebep olan hibritlerin hazırlanma yöntemini içerir. Hazırlanan MWNT/DTTC nanohibritlerin 15 dakika boyunca sürekli NIR lazer ışınımı yoluyla lokal sıcaklık artışı 92°C'ye ulaşarak dispersiyon içerisindeki *P. aeruginosa* hücreleri üzerinde %77 öldürme verimliliği sağlamıştır. Nanohibritlerin antimikrobiyal ve antibiyofilm kaplaması olarak yüzey üzerindeki fototermal aktivitesini değerlendirmek için, su bazlı poliüretan (PU) matriksine MWNT/DTTC nanohibritleri eklenmiştir. Böylece, hazırlanan MWNT/DTTC-PU nanokompozitleri sadece 3 dakika lazer ışınımı sonrasında 120°C'ye ulaşan yüksek sıcaklıklar üretmiştir. Birden fazla lazer ışınımı döngüsünden sonra, MWNT/DTTC-PU nanokompozitlerin ışıkla aktive edilen ısı üretiminde azalma gözlenmemiştir ve bu nanokompozitlerin fototermal dönüşüm açısından yeniden kullanılabilirliği kanıtlanmıştır. MWNT/DTTC-PU nanokompozitlerin yüzeye bağlanmış *P. aeruginosa* hücreleri üzerindeki antimikrobiyal aktivitesi lazer taramalı konfokal mikroskopu kullanılarak incelenmiştir.

Üçüncü bölümde, CNT'lerin ışık absorpsiyon kapasitesini geliştirmek için DNA'ların öztoplanması rehberliğinde üç ayrı tek duvarlı CNT'ün (SWNT) istenen nanoyapılara yerleştirilmesi temelli yeni bir yaklaşım geliştirdik. Özel olarak tasarlanmış üç kollu DNA bağlantısı (3WJ), SWNT'lerin yüzeyine sarılmak üzere komplementer olmayan tek zincirli kuyruklar içeren 3 adet Watson Crick çift sarmalından oluşur. DNA-3WJ nanoyapıları, SWNT'ler için dispersiyon ajanı ve bu nanotüplerin birbirlerine göre 120° açıyla kontrollü bir dallanmış yapı oluşturmak için kovalent olmayan bağlarla öztoplanmasını sağlayan sabit bir şablon görevi görür. CNT ve DNA-3WJ nanoyapılarının oluşturduğu hibritler, biyolojik ve sensör uygulamaları için SWNT'lerin floresan etiketlenmesini de mümkün kılmıştır. DNA-3WJ/SWNT nanohibritleri, aynı konsantrasyondaki tek SWNT'lere göre gelişmiş NIR absorpsiyonuna ve gelişmiş fototermal dönüşüme sahiptir. Bu iyileştirme, CNT bazlı nanomalzemelerin daha güçlü fototermal aktiviteye sahip fototermal ajanlar olarak kullanımı için değerli bir yaklaşım sunar. Dördüncü bölüm ikinci bölümün devamı olarak, CNT'lerin yüzeyinin görünür dalgada ışığı absorbe eden floroforların öztoplanmasıyla daha geniş bantta ışık hasadı yapan nanohidratların solar fototermal ajanlar olarak hazırlanması ve karakterizasyonunu içerir. Bu amaçla, CNT'lerin yüzeyi ultraviyole, görünür ve yakın kızılötesi bölgelerinde güçlü ışık absorpsiyon kapasitesine sahip birden çok floroforlar ile dekore edilmiştir. Hazırlanan CNT/Fluorofor nanohibritlerin fototermal dönüşüm verimlerini araştırmak için güneş simülatöründen elde edilen yapay güneş ışığına maruz bırakılmıştır.

ACKNOWLEDGEMENTS

First and foremost, I would like to express my deepest gratitude to my advisor, Dr. Hayriye Ünal for her academic and personal support during my time at Sabanci University. With her encouragement and continuous optimism, this thesis does not only mean a few words in my resume but also valuable experiences that I will not learn elsewhere. I am honored to be part of her research group. I would like to thank my thesis committee members, Prof. Dr. Kürşat Şendur and Prof. Dr. Sedef Tunca Gedik, for all their guidance through this process.

I am grateful to all my friends and office mates for creating a cheerful atmosphere during coffee breaks. I am particularly grateful to Adnan Taşdemir, Cem Balda Dayan, Dr. Özlem Karahan and Rıdvan Erğun for all the happy moments I have shared with them during our trip to Gaziantep, and I will not forget the great times we have spent at Sabanci. Especially, Ridvan; I can not imagine myself while I try to organize my thesis calmly. Thank you for your patience and efforts. I believe that you will find great opportunities in England than you imagine.

Special thanks go to Melike Barak for providing a fun-filled, friendly environment, and of course her delicious food! We are more than friends, we are sharing the same passions and similar goals and all these accomplishments mean something when you share it with this kind of friends. I am so grateful to have such a friend like her in my life.

None of this would be possible without the support of my family, Süleyman Altın, Mediye Altın, Berkay Altın and Ayşenur Sönmezcan. Thank you for all your sacrifices and for teaching me to be a good person before everything else but to not let people walk all over me. I will put in my best effort always to be a fair, charitable and contented person, as I learned from my grandfather Sadettin Altın. Lastly and most importantly, I am grateful to my wonderful husband. Thank you for always offering me the last bite of pizza even though you want it more than I do. Thank you for loving me unconditionally, putting my priorities before yours, being the best fellow traveller in my road. Thank you for always being there for me and your patience to be part of this part-time marriage. I can not imagine my life without you. Thank you for everything.

This thesis was funded by the Scientific and Technological Research Council of Turkey (TUBITAK) under the grant agreement number 315M235.

TABLE OF CONTENTS

ABSTRACT.....	v
ÖZET	vii
ACKNOWLEDGEMENTS	ix
LIST OF FIGURES	xii
LIST OF TABLES	xvi
ABBREVIATIONS	xvii
CHAPTER 1. INTRODUCTION	1
1.1. Photothermal Treatment for Antibiotic-Resistant Bacteria.....	1
1.1.1. Nanoparticles as photothermal agents	2
1.1.1.1. Gold nanoparticles	2
1.1.1.2. Graphene	5
1.1.1.3. Carbon nanotubes	6
1.2. Improving photothermal properties of carbon nanotubes with cyanine dyes	7
1.2.1. Interaction of cyanine dyes with DNA	8
1.2.2. Cyanine Dye Aggregates on DNA Nanotemplates	10
1.3. DNA Templated Self-assembly of SWNTs	12
1.4. Thesis Overview.....	18
CHAPTER 2. FLUOROPHORE-DECORATED CARBON NANOTUBES WITH ENHANCED PHOTOTHERMAL ACTIVITY AS ANTIMICROBIAL NANOMATERIALS	20
2.1. Introduction	20
2.2. Experimental	22
2.2.1. Materials	22
2.2.2. Preparation of MWNT and MWNT/DTTC nanohybrids	22
2.2.3. Characterization of MWNT/ DTTC nanohybrids	22
2.2.3.1. Laser activated heating in MWNT/DTTC nanohybrids	23
2.2.3.2. Laser activated antimicrobial activity of MWNT/DTTC hybrids	23
2.2.3.3. Scanning Electron Microscopy (SEM)	24
2.2.4. Preparation of MWNT/DTTC-PU Coatings	24
2.2.4.1. Laser activated heating in MWNT/DTTC-PU coatings	24
2.2.4.2. Laser activated antibiofilm properties of MWNT/DTTC-PU coatings ..	25

2.3. Results and Discussion.....	25
CHAPTER 3. DNA DIRECTED SELF-ASSEMBLY OF SINGLE WALLED CARBON NANOTUBES INTO THREE-WAY JUNCTION NANOSTRUCTURES.	35
3.1. Introduction	35
3.2. Experimental	37
3.2.1. Materials	37
3.2.2. Preparation and characterization of DNA-3WJ.....	37
3.2.3. Preparation of DNA-3WJ/SWNT nanohybrids.....	38
3.2.4. Characterization of 3WJ-DNA/SWNT nanohybrids.....	38
3.2.4.1. Atomic Force Microscopy (AFM).....	38
3.2.4.2. Scanning Electron Microscopy (SEM).....	39
3.2.4.3. Agarose gel electrophoresis	39
3.2.4.4. Fluorescence Spectroscopy.....	39
3.2.4.5. Dynamic Light Scattering (DLS).....	39
3.2.4.6. Laser activated heating in DNA-3WJ/SWNT nanohybrids.....	39
3.3. Results and Discussion.....	40
3.3.1. Preparation and characterization of 3WJ-DNA Nanostructures	40
3.3.2. Preparation and characterization of hybrids of DNA-3WJ and SWNTs.....	41
CHAPTER 4. FLUOROPHORE-DECORATED CARBON NANOTUBES AS SUNLIGHT ACTIVATING PHOTOTHERMAL AGENTS	50
4.1. Introduction	50
4.2. Experimental	52
4.2.1. Materials	52
4.2.2. Preparation of CNT/Fluorophores Nanohybrids	52
4.2.3. Characterization of CNT/Fluorophores nanohybrids	53
4.2.3.1. Sunlight activated heating in CNT/Fluorophores nanohybrids	53
4.3. Results and Discussions	54
CHAPTER 5. CONCLUSIONS	61
REFERENCES	63

LIST OF FIGURES

Figure 1. The extinction coefficient of hemoglobin and water [3].	1
Figure 2. Absorbance spectra of (a) GNPs coated with different molecular weight of amphiphilic block copolymer [11], (b) GNRs with different aspect ratios [8].	3
Figure 3. Confocal images of liver cancer cell (HepG2) irradiated by NIR laser light with respect to time [9].	4
Figure 4. Illustration of cell membrane damage before and after NIR laser irradiation of tumor cell. (A, B) the cell treated with GNRs on the membrane, (C, D) the cell treated with GNRs inside the cell [7].	5
Figure 5. TEM images of <i>Staphylococcus aureus</i> treated with GNPs. (a) before laser exposure, (b-e) after laser exposure with 100 pulses, pulse duration of 12 ns, and wavelength of 532 nm: laser fluence is 0.5 J/cm ² and 3 J/cm ² for (b, c) and (d, e), respectively and that accompanied with separate GNPs and/or GNP cluster [10].	5
Figure 6. General structure of cyanine dye [35].	8
Figure 7. Symmetrical and asymmetrical cyanine dyes [35].	8
Figure 8. Schematic representation of different binding modes of small molecules to dsDNA [40].	9
Figure 9. Splitting of the excited state based on exciton-coupling model (left) and face-to-face and end-to-end coupling for H- and J-aggregate (right) [45].	11
Figure 10. Schematic representation of ssDNA wrapped carbon nanotubes. The bases (red) are stretched out from the DNA backbone (yellow) leading to right-handed helical structure [63].	14
Figure 11. DNA origami nanostructures [66].	15
Figure 12. (a) Schematic diagram and AFM image of alkyne-functionalized DNA wrapped SWNTs in presence of copper species and bisazide linker; (b) Schematic diagram and AFM image of azide-functionalized DNA wrapped SWNTs in presence of bisalkyne linker; (c) Schematic diagram and AFM image of alkyne-functionalized DNA wrapped SWNTs and azide-functionalized DNA wrapped SWNTs in presence of copper species; (d) Schematic diagram and TEM image of SWNT network formation via by azide-alkyne click reaction [69].	16
Figure 13. Schematic illustration of linker-induced surface assembly process. (a) DNA linker and SWNT were sonicated to functionalize SWNTs; (b) DNA linker wrapped SWNTs; (c) The deposition of DNA-SWNTs on charged surface and alignment in (d)	

parallel arrays due to surface diffusion; (e) AFM image of DNA-SWNT arrays with ~22nm pitch on mica surface [70].	17
Figure 14. Schematic representation of the preparation of (a) CNT/Fluorophore and (b) DNA-3WJ/SWNT nanohybrids.	18
Figure 15. a) Schematic demonstrating the preparation of MWNT/DTTC nanohybrids. b) photographs of MWNTs sonicated in water (left) and in an aqueous solution of DTTC (right).	26
Figure 16. a) Normalized absorbance spectra of DTTC and MWNT/DTTC containing equal concentrations of DTTC. b) Absorbance spectra of MWNTs and MWNT/DTTC containing equal concentrations of MWNTs. c) Fluorescence spectra of DTTC and MWNT/DTTC containing equal concentrations of DTTC.	27
Figure 17. a) Time-temperature curves of DTTC, MWNT and MWNT/DTTC containing equal DTTC and MWNT concentrations generated by 808 nm NIR laser irradiation for 15 min. b) Time-temperature curves generated by 808 nm NIR laser irradiation of the same MWNT/DTTC nanohybrid sample for three consequent cycles.	28
Figure 18. Viability of <i>P. aeruginosa</i> cells in the presence and absence of MWNTs and MWNT/DTTC nanohybrids before and after 808 nm laser irradiation for 15 min.	30
Figure 19. Representative SEM images of <i>P. aeruginosa</i> cells alone (a, b) and <i>P. aeruginosa</i> cells in the presence of MWNT/DTTC nanohybrids (c, d). Images a and c were obtained before 808 nm laser irradiation; images b and d were obtained after 808 nm laser irradiation.	31
Figure 20. Schematic demonstrating the application of MWNT/DTTC-PU nanocomposites as antimicrobial surface coatings. Inset: Photographs of PU, MWNT-PU and MWNT/DTTC-PU nanocomposites as self-standing films.	32
Figure 21. a) Time-temperature curves of PU, MWNT-PU and MWNT/DTTC-PU films generated by 808 nm NIR laser irradiation for 5 min. b) Time-temperature curves generated by 808 nm NIR laser irradiation of the same MWNT/DTTC-PU film for three consequent cycles.	33
Figure 22. Representative laser scanning confocal microscopy images of PU (a,b) and MWNT/DTTC-PU surfaces (c,d). Images a and c were obtained before 808 nm laser irradiation; images b and d were obtained after 808 nm laser irradiation.	34
Figure 23. a) Schematic of the self-assembly of DNA-3WJ. Same color regions represent complementary sequences and black regions represent poly-G sequences b) Visualization of the agarose gel loaded with individual ssDNA strands, binary combinations of ssDNA	

strands and a mixture of all three ssDNA strands. All samples were annealed to 95°C for 5 min and cooled in ice bath c) Fluorescence titration curve demonstrating the increase in fluorescence intensity of DNA-3WJ at increasing fluorophore concentrations.	40
Figure 24. a) Schematic representation of the formation of DNA-3WJ/SWNT hybrid nanostructures b) Photographs of SWNTs ultrasonicated in water (left) and SWNTs ultrasonicated in DNA-3WJ solution.....	42
Figure 25. a) AFM topographical image of DNA-3WJ/SWNT hybrid nanostructures, b) Cross sectional analysis of representative topographical AFM (a) and SEM (b) images of DNA-3WJ/SWNT hybrid nanostructures.	43
Figure 26. a) Visualization of an agarose gel loaded with equal amounts of ssDNA/SWNT (left) and DNA-3WJ/SWNT (right) b) Average hydrodynamic diameters of ssDNA/SWNT and DNA-3WJ/SWNT hybrids measured by DLS.....	44
Figure 27. Fluorescence spectra of equal amounts of YOYO-1 i) in water (black squares) and ii) bound to DNA-3WJ/SWNT (red circles).	45
Figure 28. Schematic representation of the hypothesized mechanism of formation of DNA-3WJ/SWNT nanostructures with the post-annealing method.....	46
Figure 29. a) Visualization of an agarose gel loaded with DNA-3WJ/SWNT hybrid nanostructure prepared with pre-annealing (left) and post-annealing (right) methods. b) Average hydrodynamic diameters of DNA-3WJ/SWNT nanostructure prepared with pre-annealing (left) and post-annealing (right) methods.	47
Figure 30. a) A representative AFM image of DNA-3WJ/SWNT nanostructures prepared with the post-annealing method. b) A representative SEM image of DNA-3WJ/SWNT nanostructures prepared with the post-annealing method. c) A schematic representation of the potential mechanism of formation of the network structure when the post-annealing method is used.	48
Figure 31. a) Time-temperature curves of SWNT and DNA-3WJ/SWNT containing equal SWNT concentration generated by 808 nm NIR laser irradiation for 15 min. b) Time-temperature curves generated by 808 nm NIR laser irradiation of the same DNA-3WJ/SWNT nanohybrid sample for two consequent cycles.	49
Figure 32. Experimental setup for the measurement of photothermal conversion by solar simulator.	54
Figure 33. Absorbance spectra of DWNT/Disc ₂ (1)-Disc ₂ (5)-DTTC and MWNT/Disc ₂ (1)-Disc ₂ (5)-DTTC nanohybrids.....	55

Figure 34. a) Normalized absorbance spectra of Disc₂(1)-Disc₂(5)-DTTC and MWNT/Disc₂(1)-Disc₂(5)-DTTC in the range of Disc₂(1) absorption containing equal concentration of fluorophore solution. b) Normalized absorbance spectra of Disc₂(1)-Disc₂(5)-DTTC and MWNT/Disc₂(1)-Disc₂(5)-DTTC in the range of Disc₂(5) absorption containing equal concentration of fluorophore solution. c) Normalized absorbance spectra of Disc₂(1)-Disc₂(5)-DTTC and DWNT/Disc₂(1)-Disc₂(5)-DTTC in the range of Disc₂(1) absorption containing equal concentration of fluorophore solution. d) Normalized absorbance spectra of Disc₂(1)-Disc₂(5)-DTTC and DWNT/Disc₂(1)-Disc₂(5)-DTTC in the range of Disc₂(5) absorption containing equal concentrations of fluorophore solution..... 56

Figure 35. Absorbance spectra of DWNT and DWNT/(TO-PRO-1)-(TO-PRO-3)-Hoechst-PI nanohybrids containing equal concentration of DWNTs. (a), and absorbance spectra of (TO-PRO-1)-(TO-PRO-3)-Hoechst-PI and DWNT/(TO-PRO-1)-(TO-PRO-3)-Hoechst-PI containing equal concentration of fluorophore solution in the range of corresponding fluorophore absorption..... 57

Figure 36. Fluorescence spectra of Disc₂(1)-Disc₂(5)-DTTC and MWNT/Disc₂(1)-Disc₂(5)-DTTC containing equal concentration of fluorophore solution..... 58

Figure 37. Time-temperature curves of (a) DWNT, DWNT/ Disc₂(1)-Disc₂(5)-DTTC and Disc₂(1)-Disc₂(5)-DTTC, (b) MWNT, MWNT/ Disc₂(1)-Disc₂(5)-DTTC and Disc₂(1)-Disc₂(5)-DTTC, (c) DWNT, DWNT/(TO-PRO-1)-(TO-PRO-3)-Hoechst-PI and (TO-PRO-1)-(TO-PRO-3)-Hoechst-PI containing equal fluorophores and CNT concentration generated under 1 sun illumination for 15 min..... 59

Figure 38. Time-temperature curves obtained under one sun illumination of the same DWNT/ Disc₂(1)-Disc₂(5)-DTTC and MWNT/ Disc₂(1)-Disc₂(5)-DTTC nanohybrid samples for two consequent cycles..... 60

LIST OF TABLES

Table 1 Sequences of ssDNA utilized for the self-assembly of DNA-3WJ	37
Table 2 The fluorophores that have been utilized to create sunlight activated CNT nanohybrids.....	52

ABBREVIATIONS

CNT:	Carbon nanotubes
SWNT:	Single walled carbon nanotubes
DWNT:	Double walled carbon nanotubes
MWNT:	Multi walled carbon nanotubes
DNA:	Deoxyribonucleic acid
dsDNA:	Double Stranded DNA
ssDNA:	Single Stranded DNA
GNP:	Gold nanoparticle
GNR:	Gold nanorod
LSPR:	Localized surface plasmon resonance
NIR:	Near Infrared
TEM:	Transmission electron microscopy
SEM:	Scanning electron microscopy
DLS:	Dynamic Light Scattering
PU:	Polyurethane

CHAPTER 1. INTRODUCTION

1.1. Photothermal Treatment for Antibiotic-Resistant Bacteria

Antibiotic resistance has become one of the most important global problems on public health over the past several decades caused by the misuse and overuse of antibiotics, reaching 100 000 tons each year worldwide, over the past several decades [1, 2]. Pathogenic bacteria which have resistance to current antibiotics such as *Staphylococcus aureus* or *Pseudomonas aeruginosa*, are responsible for enormous economical and medical losses. Although several research studies are embarking on a quest to find new antibiotics, it is only a band-aid solution in the fight against bacteria since they will develop different mechanisms to counteract the new antibiotics sooner or later. Scientists are forced to find new alternatives for conventional biochemical treatment and provide new approaches to this global problem.

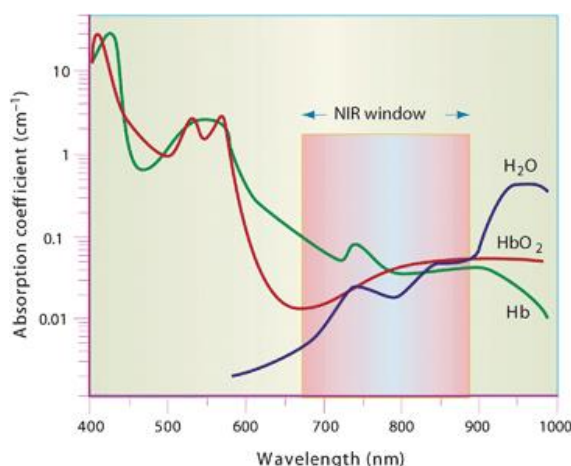


Figure 1. The extinction coefficient of hemoglobin and water [3].

Utilization of well-designed nanoparticles as photothermal agents presenting light-induced heating is a phenomenon that provides an alternative treatment for bacterial infections. Photothermal agents are capable of inducing local temperature elevations by irradiation light. They can absorb the light and convert this energy into heat. These local temperature elevations cause the lysis of cells due to protein denaturation, DNA damage and oxidative stress [4]. A key factor when using photothermal agents for biological application is adjusting their optical properties to absorb in the desired wavelength range called the biological window which is the Near Infrared (NIR) region of the spectrum. While hemoglobin and water show strong absorption in the visible and infrared range,

their very minimal absorption in the NIR region allows deeper penetration of light into tissue (Figure 1) [3, 5, 6]. The elimination of undesired absorption allows the control of temperature elevations and minimization of the damage to surrounding healthy cells. While nanoparticle-based hyperthermia has been frequently used in cancer therapy, we and others adapted this technique as an effective approach for killing bacteria [4, 7, 8].

Russell et al. showed that most of the pathogenic bacteria are unable to survive above 50°C due to cell membrane damage [5]. For this reason, temperatures under laser irradiation via photothermal agent must exceed 50°C to kill the antibiotic resistant bacteria. The effect of temperature can be shown as irreversible morphology change of the cell. Other causes of cell death at elevated temperatures include DNA damage, protein denaturation, enzyme inactivation, oxidative stress, bubble formation and/or melting of attached nanoparticle on the cell wall [7, 9, 10]. In general, more than one reason are responsible for the cell death at elevated temperatures.

1.1.1. Nanoparticles as photothermal agents

1.1.1.1. Gold nanoparticles

Utilization of nanoparticles as photothermal agents provides a selective and powerful treatment under specific condition. The localized surface plasmon resonance of metal particles make them promising candidate for this purpose. Their free surface electrons are responsible for collective and coherent oscillation accompanied by conversion of light energy into heat [6]. Gold nanoparticles (GNPs) are well-known metallic photothermal agents due to their strong visible absorption capacity. The effectiveness of these metallic nanoparticles depends on their size, shape and aggregation behavior. While dispersed gold nanoparticles show relatively narrow absorption at 520 nm accompanied with limited optical penetration depth, their aggregated forms demonstrate enhanced photothermal conversion. He et al. indicated that the localized surface plasmonic resonance (LSPR) peak of copolymer coated assembled GNPs shifted to longer wavelengths in the NIR range due to plasmonic coupling of GNPs. As demonstrated in Figure 2a, assembled GNPs introduce a new plasmonic peak at around 730 nm besides the red shift [11]. This phenomenon provides an important tool to tune absorption characteristics of gold particles in a desired wavelength range on behalf of several applications.

Another way to manipulate the localized surface plasmon frequency of GNPs in terms of optical properties is their morphology. Many studies have demonstrated that more complex geometries such as sphere, rod, or stars modified the plasmonic oscillation of nanoparticles distinct from their original shape. Huang et al. employed gold nanorods (GNRs) to visualize and destruct cancer cells with photothermal method. The extinction spectrum of these nanorods divided into two plasmon modes arising from the oscillation of electron along the long and short dimension of GNRs called longitudinal and transverse mode, respectively (Figure 2b). By changing the aspect ratio, the longitudinal absorption peaks have shifted toward the biological window in enhancement of photothermal efficiency of particles especially for in vivo treatment [8].

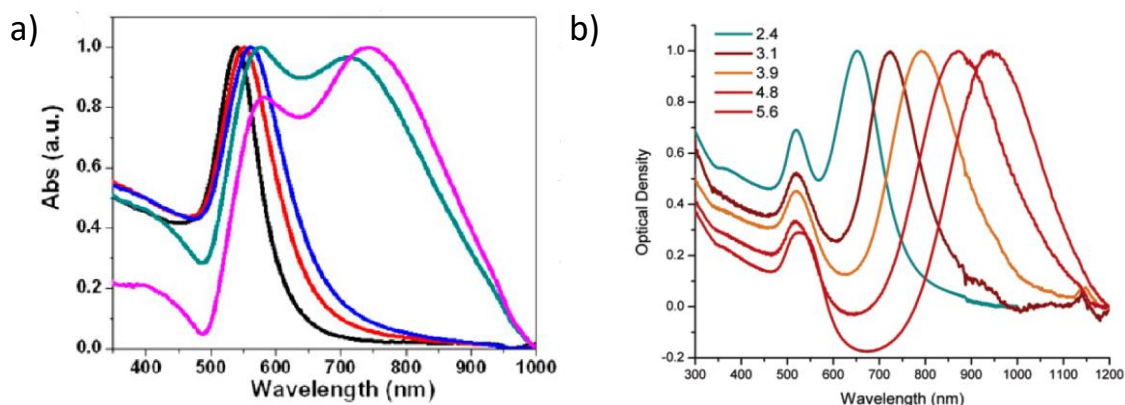


Figure 2. Absorbance spectra of (a) GNPs coated with different molecular weight of amphiphilic block copolymer [11], (b) GNRs with different aspect ratios [8].

One of the factors that needs to be optimized to perform in-vitro photothermal treatment at maximum efficiency is where the photothermal agent is located with respect to the bacterial cells. The optimum location is an important but controversial issue in the literature. Zhou et al. compared the photothermal efficiency of GNRs are attached to cells (intracellular treatment) and GNRs exposed to cells in solution (extracellular treatment) [9]. While 130 s of irradiation is sufficient to kill the cancer cell within the spot area for intracellular therapy, cells required irradiation for 190 s to reach the same result for extracellular therapy (Figure 3). On the contrary, Tong et al. claimed that the threshold laser power to cause irreversible membrane blebbing for GNRs on the cell membrane is an order of magnitude less than the laser power required for intercellular incorporation of GNRs with cells (Figure 4) [7]. They explained the possible reasons of why extracellular

manipulation of cells is a more favorable treatment method for photothermal therapy. These three factors point out the advantages of utilization photothermal nanoparticles located outside the cells for higher killing efficiency: (i) The cell membrane damage caused by irradiation of laser light is a decisive and direct method to kill them, (ii) GNRs accumulation on the cell membrane enables concentration of the photothermal effects in the certain area, (iii) Intense hyper-thermic effects consequence of larger temperature zone around the laser focus can be achievable due to low thermal conductivity of the cell membrane [12].

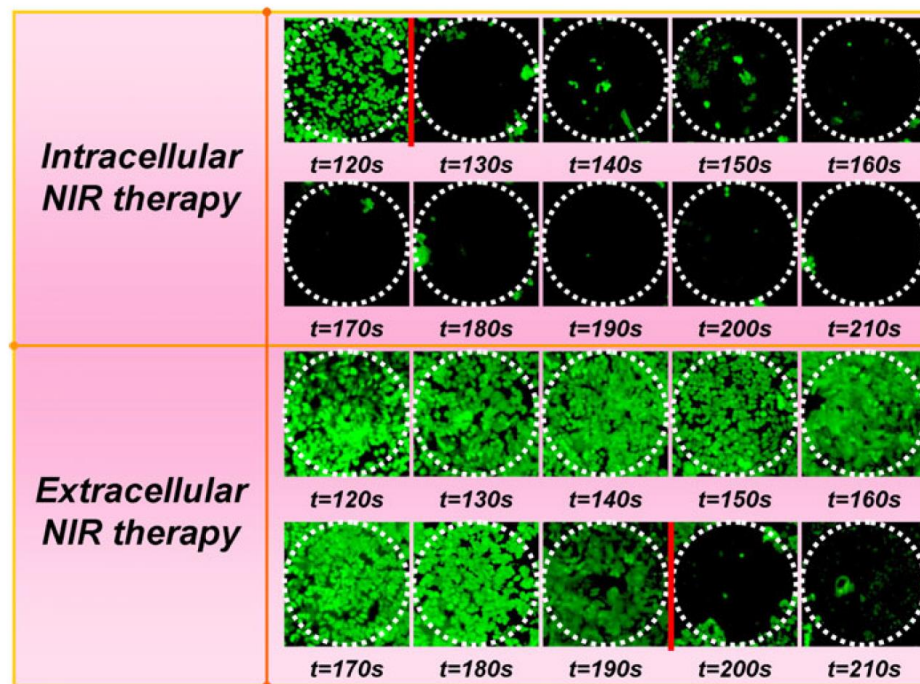


Figure 3. Confocal images of liver cancer cell (HepG2) irradiated by NIR laser light with respect to time [9].

Another factor determining the efficiency for photothermal therapy is the mode of the laser utilized for irradiation. Two laser operating modes exist to create local temperature elevations in principal. The continuous laser induces the heat dissipation around the nanoparticles by diffusion while the pulse laser causes the multiphoton absorption in restricted time resulting in localized overheating and bubble formation [10, 13, 14]. It allows the tuning of the treatment condition depending on the desired outcome. The destructive effects of cluster formation and laser fluence on bacterium can be seen in Figure 5 which is the consequence of high temperature elevation and membrane blebbing. Zharov et al. were pioneers in pointing out the utilization of GNPs to cause physical

damage on bacteria with photothermal treatment [10]. TEM images proved that high laser energy and/or formation of GNP clusters induced deeper penetration of these particles into the cell wall resulting in irreversible cell membrane damage. It triggered the destruction of bacterium represented by dashed line in Figure 5.

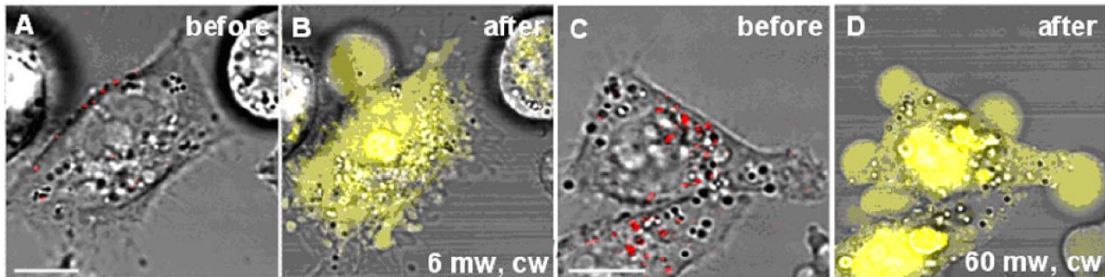


Figure 4. Illustration of cell membrane damage before and after NIR laser irradiation of tumor cell. (A, B) the cell treated with GNRs on the membrane, (C, D) the cell treated with GNRs inside the cell [7].

1.1.1.2. Graphene

Wu et. al proposed graphene as a promising photothermal agent to kill both gram-negative (*E. coli*) and gram-positive (*S. aureus*) bacteria [15]. They functionalized reduced graphene oxide with superparamagnetic nanoparticles and glutaraldehyde. While glutaraldehyde cross-linked with bacterial cell wall for efficient capturing, magnetic graphene oxide accumulated under the external magnet during NIR laser irradiation. It significantly diminished the survival rates of gram-positive and gram-negative bacteria. Moreover, Yang et. al. and Robinson et. al. demonstrated the noncovalent functionalization of nanographene oxide with polyethylene glycol as a NIR absorbing photothermal agent for tumor destruction in vivo and in vitro, respectively [16, 17].

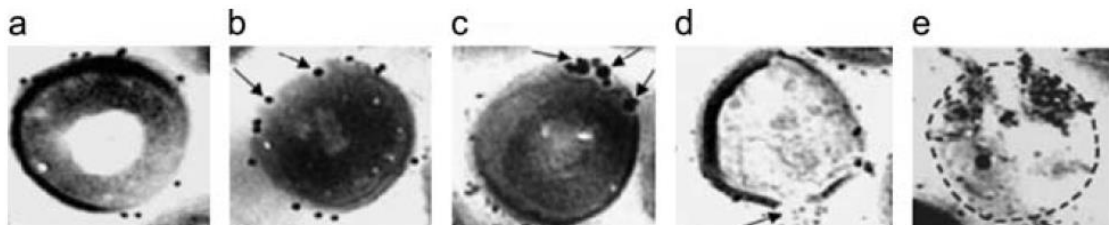


Figure 5. TEM images of *Staphylococcus aureus* treated with GNPs. (a) before laser exposure, (b-e) after laser exposure with 100 pulses, pulse duration of 12 ns, and wavelength of 532 nm: laser fluence is 0.5 J/cm^2 and 3 J/cm^2 for (b, c) and (d, e), respectively and that accompanied with separate GNPs and/or GNP cluster [10].

1.1.1.3. Carbon nanotubes

In recent years, carbon nanotubes (CNT) have been successfully utilized as photothermal agents to kill antibiotic-resistant bacteria [18-21]. They have strong potential as photothermal agents because of their lower cost and the enhancement of their biocompatibility by surface functionalization [4]. Indeed, CNTs have the edge over GNPs thanks to their high photostability and thermal conductivity. These properties provide the utilization of these particles for in vivo application without concerning the melting or decomposition of nanoparticles due to excessive heat generation [22, 23]. Despite these advantages, the major obstacle for using CNTs as light activated nanoparticles is their lower NIR absorption with respect to GNPs [24]. The photothermal properties of CNTs can be improved by enhancing their NIR light absorption capacity leading to higher light absorption and heat generation capacity for efficient killing of bacteria and cancer cells. This enhancement makes them attractive alternatives to GNPs and graphene. The use of CNT as a photothermal agent in vitro has also been investigated which includes the surface functionalization of CNTs to enhance their solubility, biocompatibility and target specificity [25, 26]. The diameter, length and surface characteristics of CNTs can be optimized to improve the light-to-heat conversion efficiency which make it a flexible and appealing candidate for both in vivo and in vitro studies [4].

Their photothermal conversion mechanism is slightly different than the mechanism of metallic nanoparticles. The optically induced Van Hove transitions are responsible for the heating of CNTs which are accompanied by the plasmon resonance of free carriers which is originated from π bonds between the carbon atoms. Their vibration energy is transferred to the surrounding in the form of heat through the electron-phonon relaxation [27, 28]. While heat generation mechanism of GNPs is revealed only when they are irradiated within the surface plasmon resonance wavelength, the heat conversion of CNTs does not depend on the wavelength; they absorb light in a wide spectral range [29]. In this respect, even though GNPs show higher conversion efficiency compared to CNTs, wavelength independency of CNTs enable deeper tissue penetration and tunable photothermal treatment. The important advantages of CNTs over gold nanorods in terms of photothermal therapy was demonstrated by the comparative study of Robinson et al. [30]. They indicated that gold nanorods required 10-fold higher doses and 3-fold higher laser power to thermally destroy the tumor cells than required by CNTs. Their 1D electronic structure, large Stokes shift between excitation and emission bands and low

quantum yield make them an outstanding candidate for near-infrared imaging and tumor ablation.

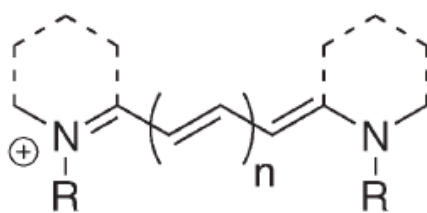
The excitation/emission wavelength and light-to-heat conversion efficiency strictly depends on the chirality and metallic or semiconducting properties of CNTs [4, 30]. The chiral separation could improve the absorption intensity in specific wavelength ranges of laser light. Moreover, the ability to convert light into heat is also attributed to their different density of states at Fermi level arising from metallic or semiconducting CNTs.

Ghosh et al. showed a new method to enhance the photothermal conversion capacity via DNA encasement of MWNTs [28]. By using this method, the degree of aggregation could be minimized. It facilitates the consistency between the wavelength of laser and the resonance wavelength of CNT accompanied by improved light-to-heat conversion.

In this thesis, noncovalent functionalization of CNTs was investigated to improve their photothermal properties for killing bacteria. For this purpose, we introduced two methods to enhance the light absorption capacity of CNTs with the aim of increasing the amount of light absorbed by prepared photothermal agents. These methods focused on i) the decoration of MWNTs surface with arrays of fluorophores and ii) the self-assembly of three individual SWNTs into a DNA three-way junction. For the first method, cyanine dyes were utilized for the functionalization of MWNTs.

1.2. Improving photothermal properties of carbon nanotubes with cyanine dyes

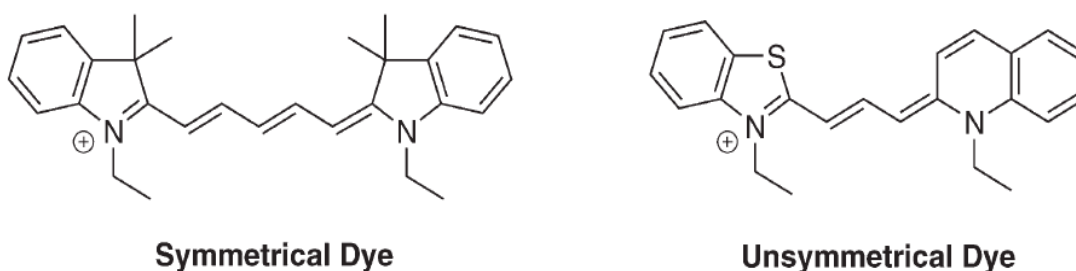
Cyanine dyes are remarkable colored compounds introduced by Williams in 1856 which have been widely utilized ranging from biological applications to inorganic semiconductor materials [31]. The typical structure of cyanine dye consists of two nitrogen atoms that carry a delocalized positive charge between them, and these nitrogen atoms are connected to each other with an odd number of carbon atoms (Figure 6). R-groups located at different positions on heterocycles represents the substituents that determine the physical properties and electronic structure of cyanine dyes such as aggregation and solubility, and electronic transition, respectively. The most common reason to modify the spectroscopic characteristics of cyanine dyes is to increase the Stoke's shift of the compounds for wavelength tuning [32-34]. Their large extinction coefficient and moderate fluorescence quantum yield make them promising candidate as fluorescent probes, photosensitizers and stains.



Generic Cyanine Dye

Figure 6. General structure of cyanine dye [35].

Symmetrical and asymmetrical cyanine dye are categorized according to the symmetry of their chromophore groups, which consist of identical or different heterocycles linked at the same or a different position (Figure 7). One of the most important differences between symmetrical and unsymmetrical dye is their fluorescence properties [35]. The unsymmetrical dyes showed strong fluorescence upon binding to nucleic acids, and negligible fluorescence when free in aqueous solution. On the other hand, the symmetrical cyanine dyes have been widely used as fluorescent labels and probes for DNA detection.



Symmetrical Dye

Unsymmetrical Dye

Figure 7. Symmetrical and asymmetrical cyanine dyes [35].

1.2.1. Interaction of cyanine dyes with DNA

Intercalation and minor groove binding are well-known binding modes between DNA and small molecules (Figure 8) [36-38]. Insertion into the minor groove requires Van der Waals interactions with the walls of minor groove resulting in limited flexibility because the binder molecule turns around the central axis of the helix [39]. Intercalators are inserted between the base pairs of DNA via cationic molecules on the ring system or substituents of the dye molecule. Intercalators present complementarity to DNA in terms of shape and electrostatic force. Intercalator needs a binding pocket between adjacent

base pairs that creates distortion of DNA. On the other hand, the groove binders have more contact points with helix and twist to follow the groove unlike the intercalators.

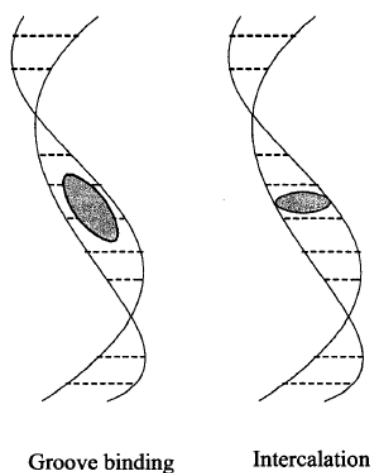


Figure 8. Schematic representation of different binding modes of small molecules to dsDNA [40].

DNA intercalators are encountered mostly for detection and quantitation of DNA due to their unique photophysical properties. When hydrophobic dye molecules enter between adjacent base pairs of DNA, π -stacking interactions with the aromatic heterocycles of the bases occur. In comparison with the minor groove binders bound to DNA, intercalators contact two base pairs with little or no twist. On the other hand, when the bridge length between two aromatic rings of intercalators is extended, the structure of intercalators resembles minor groove binders resulting in more complex binding behavior with DNA [41].

The heterocycles and the length of the methine bridge control the absorption and emission maximum of asymmetrical cyanine dyes. Intercalation into DNA results in a red shift in absorption maximum and a blue shift in fluorescence emission since conformational mobility diminishes, and the radiative decay becomes energetically favorable road to ground state in the presence of DNA. It means that fluorescence quantum yield enhancements of more than 3000-fold can be detected upon binding to DNA [42]. In contrast, when these dyes are free in aqueous solution, the nonradiative relaxation of excited electron via rotation in the methine bridge connecting the heterocycles results in very low fluorescence [43, 44].

The most important structural feature of minor groove binders is their conformational flexibility which allows them to adjust themselves according to the curvature of DNA helix. A positive charge, curvature and hydrogen bonding are other structural characteristics of these dyes. When a cationic charge facilitates electrostatic interaction with the phosphate-sugar backbone, van der Waals interactions with the floor of the minor groove is formed by a donor and C-H groups. Dimerization in the minor groove is the other specific DNA binding mode that indicates a collaborative work where the dye monomer in the minor groove promotes the binding of a second dye to form the dimer. Monomeric binding between cyanine dye and the walls of the minor groove through van der Waals interactions causes more energetic penalty compare to the π -stacking interaction between dyes. Therefore, the driving force for the binding of the first molecule is merely related to hydrophobicity of the dye because suitable van der Waals contact between the nonplanar deoxyribose sugar of DNA wall and the planar aromatic rings of cyanine dyes do not exist for dimerization of cyanine dyes [45]. Dimerization as a favorable binding mode results in distortion of the DNA to accommodate the dimer while an energetic penalty and the stability issues of complex are generated. These problems are reduced with hydrogen bond, electrostatic attractions and van der Waals contacts. In addition to that, dimerization is highly sequence selective process because the polarizability and hydrophobicity of aromatic rings determine the dimerization tendency of cyanine dyes [46]. Formation of cyanine dye dimers in the presence of DNA brings about a shift in the absorption maximum to either shorter or longer wavelength depending on the orientation of two monomers [47, 48].

1.2.2. Cyanine Dye Aggregates on DNA Nanotemplates

Cyanine dyes are generally found in an aggregate form rather than isolated monomers and these aggregates display very distinct photophysical and photochemical properties compared to their monomeric analogues. According to previous studies, DNA has been used as a scaffold to organize the assembly of cyanine dyes for promoting supramolecular aggregates where their sizes can be controlled by the length and width of the DNA template [35, 40, 47-49]. The hydrophobicity and polarizability of dyes are the driving forces for the formation of the cyanine dye aggregates through the π -stacking interactions.

Cooperative propagation of the aggregates is similar to the dimerization. After first dimer is bound within the minor groove, assembly of additional dimers directly adjacent to the first facilitates the propagation step. Assembly of the DNA-templated dye aggregates is terminated at the end of the template or when the new sequence does not promote the dimerization. Formation of aggregates in solution shows considerable difference in absorption band due to the coupling of transition moments of dye molecules [50-52]. These alterations have been observed in the UV-VIS spectrum as hypsochromic shifted H-bands and bathochromic shifted J-bands. For H-aggregates, a plenty of van der Waals interactions is provided by unsubstituted dye molecules resulting in attenuated water exposure. On the other hand, J-aggregate formation depends on electrostatic and/or static factors originating from the substituent on the dye structure. The parallel dye molecules are assembled with the intradimer (face to face) and interdimer (end to end) couplings as it shown in Figure 9. Face to face and end to end assembly of dimer causes to split the excitation state based on molecular exciton coupling theory. There is little or no offset between the two dyes in H-aggregates, and the electronic transition to upper energy state is allowed with parallel transition moments leading to blue shifts, J-aggregates show the electronic transition to lower state with perpendicular transition moments resulting in a red shift in the absorption spectrum. The intradimer coupling between two dyes in a dimer includes more orbital overlap compared with the interdimer coupling between dyes in adjacent dimers.

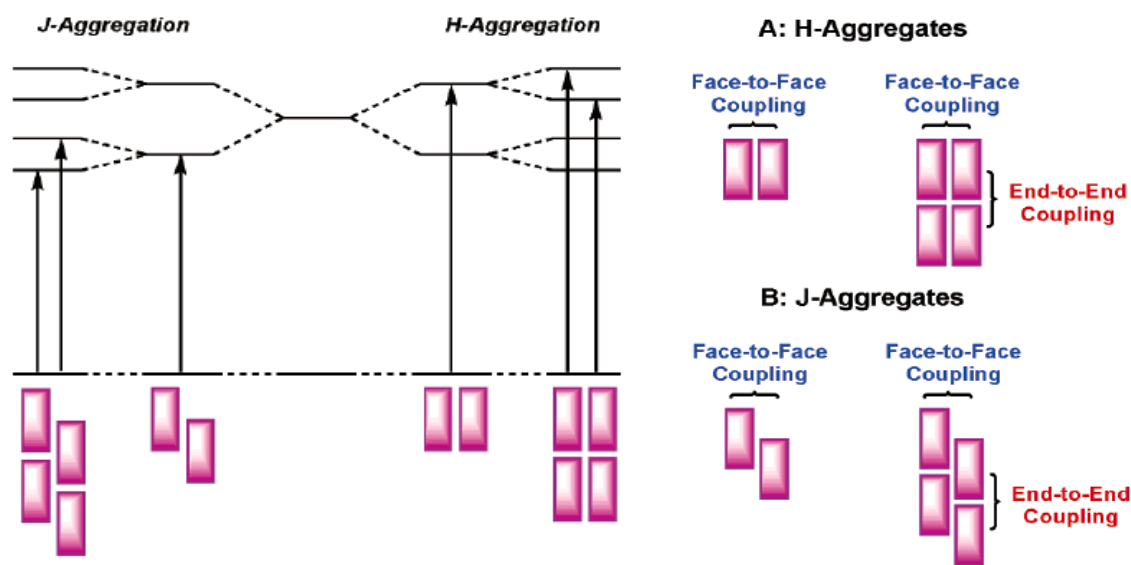


Figure 9. Splitting of the excited state based on exciton-coupling model (left) and face-to-face and end-to-end coupling for H- and J-aggregate (right) [45].

Several factors related to the cyanine dyes affect the dimerization and aggregates on DNA such as the length of polymethine bridge, the type and N-substitution of the heterocycle. Hannah and Armitage established that the cationic, anionic and branched substituents on the heterocycles have the negative influence for the dimerization and aggregation of cyanine dyes [45]. The positive or negative charge on the structure causes the electrostatic repulsion originating from dye molecules or DNA templates. In addition to that, the length of the polymethine bridge has a strong impact on the tendency of dimerization because there is a linear relationship between the bridge length, hydrophobicity and polarizability of cyanine dyes in aqueous solution [53].

In a previous study, Cavuslar and Unal reported a valuable method to prepare CNT/fluorophore nanohybrids with the purpose of fluorescent labelling of CNTs for biomedical applications and investigating their absorption capacity in desired spectral ranges [54]. As a continuation of this study, we herein report the self-assembly of cyanine dyes on the surface of CNTs to enhance the light absorption and heat generation capacity of CNTs resulting in efficient photothermal agents. The cyanine dyes used in this work have a strong affinity for double-stranded DNA (dsDNA) through different binding modes. In the light of this information, we hypothesized that these dyes can also form π - π stacking interactions with the sp^2 hybridized structure at the sidewalls of CNTs through their aromatic planar structure that is similar to the intercalation of the same dyes between adjacent base pairs of dsDNA. The interaction between CNTs and cyanine dyes may also promote the formation of supramolecular aggregates on the surface of CNTs in a similar fashion to DNA templated aggregates.

1.3. DNA Templated Self-assembly of SWNTs

Carbon nanotubes are man-made one-dimensional materials with unique optical, thermal and mechanical properties utilized in various applications ranging from transportation to biosensing [55-57]. The poor solubility of CNTs in aqueous and non-aqueous solution needs to be controlled to achieve their unique mechanical and electrical properties for several applications. These nanotube bundles are originated from strong interaction between CNTs due to van der Waals forces. The physical interference with sound waves and covalent sidewall functionalization of carbon nanotubes have been used to handle their agglomeration problem, even though these types of manipulations on CNTs can cause unavoidable structural defects and irreversible alteration of electronic properties [58-60]. Non-covalent interaction between the nanotubes and amphiphilic molecules is an

efficient alternative method to avoid these negative side effects. While the hydrophilic groups of amphiphilic molecules are in interaction with the solvent molecules to improve the solubility, the aromatic hydrophobic groups lie on the surface of CNTs [61]. As deoxyribonucleic acid (DNA) provides all these hydrophilic and hydrophobic requirements with its aromatic nucleotide bases and sugar-phosphate backbone, it acts as a useful dispersing agent for CNTs.

DNA is a linear biopolymer consisting of a sugar-phosphate backbone and two standard base pairs; Adenine (A) connected to Thymine (T) and Guanine (G) connected to Cytosine (C) with the help of hydrogen bond [62]. Two complementary single strands of DNA can link together to form a well-known DNA double helix by predictable Watson-Crick base pairing. This process is known as hybridization. In the typical right-handed helices (B-DNA), the distance between adjacent base pairs is approximately 0.34 nm, and the diameter of helix is ~ 2 nm with a helical repeat of 10.5 base pair per turn. The structure and conformation of DNA can be controlled by the sequence design through their ability to recognize complementary sequence. This phenomenon underlies the structural DNA nanotechnology.

The driving forces leading to helical wrapping of CNTs with DNA are originated from non-covalent interactions between these molecules via Van der Waals and electrostatic forces, hydrogen bonds, and π -stacking interactions [63]. Flexible sugar-phosphate backbone of DNA facilitates the connection between ssDNA bases and CNTs by finding low energy conformation. During the interaction, the bases are connecting units between DNA and nanotubes while the DNA backbone exposes to water [64]. The binding free energy between two nanotubes diminishes by wrapping CNTs with DNA that explains why these nanotubes favor to interact with DNA rather than to associate with each other. The similar effect can be seen for hybrids of CNTs with both single stranded DNA (ssDNA) or double stranded DNA (dsDNA). The intramolecular stacking between dsDNA and CNT is less favorable than π -stacking interaction of ssDNA and CNT. It shows that surface coverage is decreased during the hybridization with dsDNA while ssDNA is wrapping around CNTs.

DNA is a useful tool for CNTs to obtain high dispersion efficiency and non-covalently functionalize its outer surface without disrupting their unique electrical properties. The sorting of nanotubes by electronic structure is an important application of DNA/CNT nanohybrids [64, 65]. A negative charge density is introduced on the surface of CNTs via

the phosphate groups of DNA/CNT hybrids. The surface charge of hybrids is altered under the same condition in case of using metallic or semiconducting CNTs because the hybrid with metallic nanotube should possess less surface charge due to opposite charge. Zheng et. al. demonstrated that ion exchange chromatography can be used to separate these nanohybrids into metallic and semiconducting nanotubes [64].

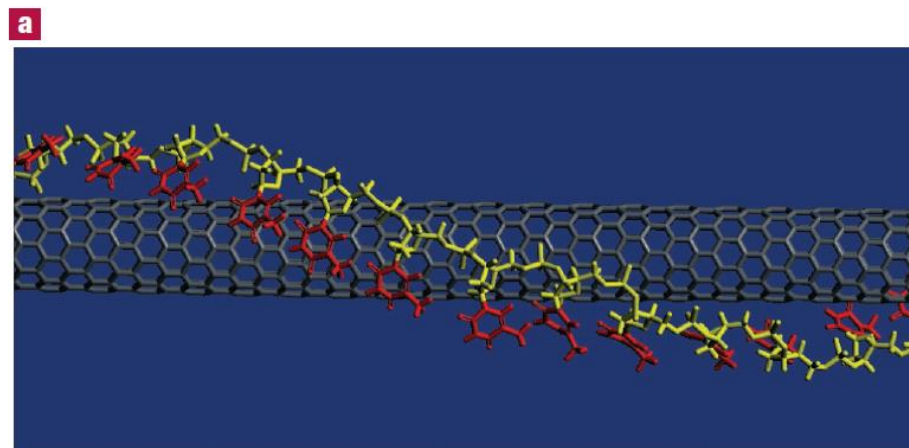


Figure 10. Schematic representation of ssDNA wrapped carbon nanotubes. The bases (red) are stretched out from the DNA backbone (yellow) leading to right-handed helical structure [63].

Since DNA origami was first introduced by Rothemund in 2006, his technique has attracted enormous attention from the scientific community [66]. He was able to fold DNA into predetermined 2D structures such as triangle, rectangle, star or smiley face, as shown in Figure 11. In this technique, a long single stranded scaffold is folded back and forth into the desired shape by raster-filling, and the hundreds of short oligonucleotides called stable strands are utilized to hold the shape together. After his study, Shih's group made the next breakthrough by constructing 3D nanostructures which are composed of honeycomb lattice [67]. One outstanding purpose of constructing DNA origami template is their ability to organize nanomaterials and biomaterials with nanometer resolution. This is one of the most appealing advantages of DNA-directed self-assembly method that enables to control distance-dependent interaction between the nanoobjects. The distance dependency of some properties is an important concept for the construction of plasmonic structure and biosensing application. For instance, DNA origami has been used to position gold nanoparticles on a triangular DNA template [68].

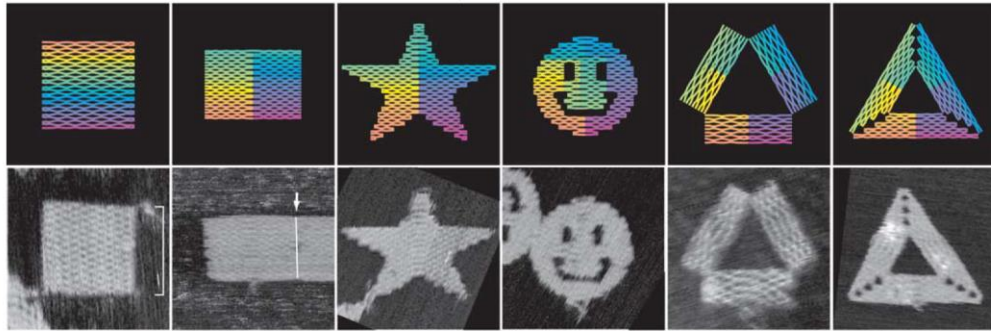


Figure 11. DNA origami nanostructures [66].

The concept of DNA origami and favorable DNA/CNT interactions have been successfully applied for the formation of DNA based self-assembled CNT nanostructures. McMorro et al. employed alkyne or azide functionalized DNA wrapped SWNTs to constitute network and 2D structures by the assembly of CNTs through copper coordination and azide-alkyne click reaction [69]. According to their AFM and TEM results, the driving force of SWNTs assembly was the functional group on ssDNA. The side-to-side interactions was formed during the reaction by the addition of copper species and complementary linker. As shown in Figure 12, the change in reaction condition enabled minimization of random crossing or star-like assemblies and variation of the number of SWNTs per assembly. Interestingly, alkyne-functionalized DNA wrapped SWNTs and azide-functionalized DNA wrapped SWNTs interacted with each other and formed 1,2,3-triazole junction between parallel SWNTs while sodium ascorbate was used as a reducing agent. This reaction is known as copper catalyzed azide alkyne cycloaddition (click chemistry). The formation of 1,2,3 -triazole junction resulted in a network formation and increased bundling of nanotubes accompanied by a higher stability than other 2D structures.

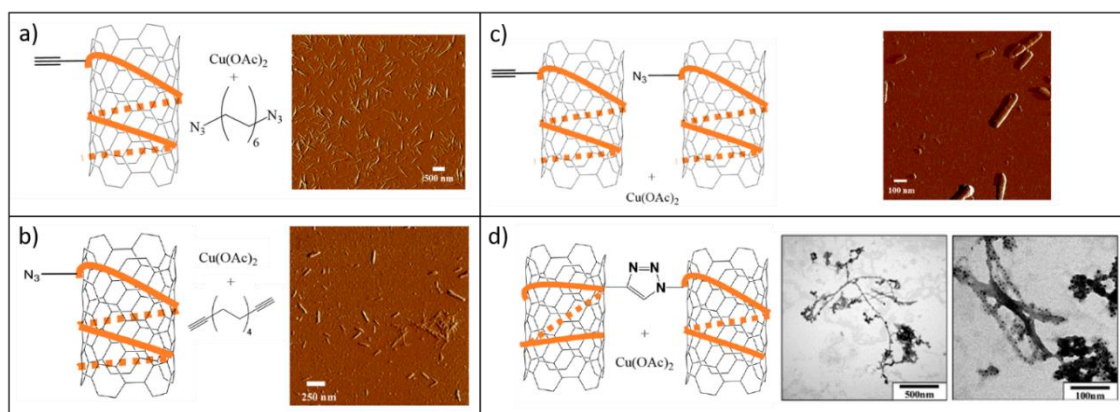


Figure 12. (a) Schematic diagram and AFM image of alkyne-functionalized DNA wrapped SWNTs in presence of copper species and bisazide linker; (b) Schematic diagram and AFM image of azide-functionalized DNA wrapped SWNTs in presence of bisalkyne linker; (c) Schematic diagram and AFM image of alkyne-functionalized DNA wrapped SWNTs and azide-functionalized DNA wrapped SWNTs in presence of copper species; (d) Schematic diagram and TEM image of SWNT network formation via by azide-alkyne click reaction [69].

Although utilization of self-assembled DNA templates to organize the nanoparticles has several advantages compare to top-down approaches, it has also significant shortcomings. The cost, complexity and limited size of DNA templated nanostructures required the new methods to create highly ordered structures which combine top down and bottom up approaches. Han et al. introduced linker-induced surface assembly (LISA) method to align SWNTs with high packing density in parallel arrays [70]. The assembly procedure is summarized in Figure 13. The duplex spacer and sticky ends of DNA linkers employed to keep uniform pitch between the adjacent SWNTs which induce parallel alignment of the nanotubes through surface diffusion. The resulting DNA scaffold enables further modifications for a wide variety of applications such as bio-molecular sensing, tissue engineering, arrangement of fluorescent dyes into defined arrays or drug delivery.

DNA hydrogels are an attractive concept of DNA self- assembly composed of three-dimensional branched DNA nanostructures [71, 72]. These hydrogels can be modified with metallic nanoparticles, protein and quantum dot to impart more versatility and functionality [73-75]. Cheng et al. indicated that DNA-SWNT hybrid hydrogel showed the liquid to gel transition with the formation of i-motif structures as pH decreased below

6.3 [76]. SWCNTs wrapped with specially designed DNA containing i-motif tail was utilized as a crosslinker between linear DNA assembly structure to form the hybrid hydrogel. In addition, the change in the concentration of DNA wrapped SWNTs was strongly correlated with the mechanical properties of the hydrogel. Their previous study showed that the strength of DNA hydrogels also exhibits temperature dependence [73]. This method allows to the design of multifunctional, pH or temperature responsive DNA-based hydrogels for a wide range of applications such as tissue engineering scaffold and drug delivery.

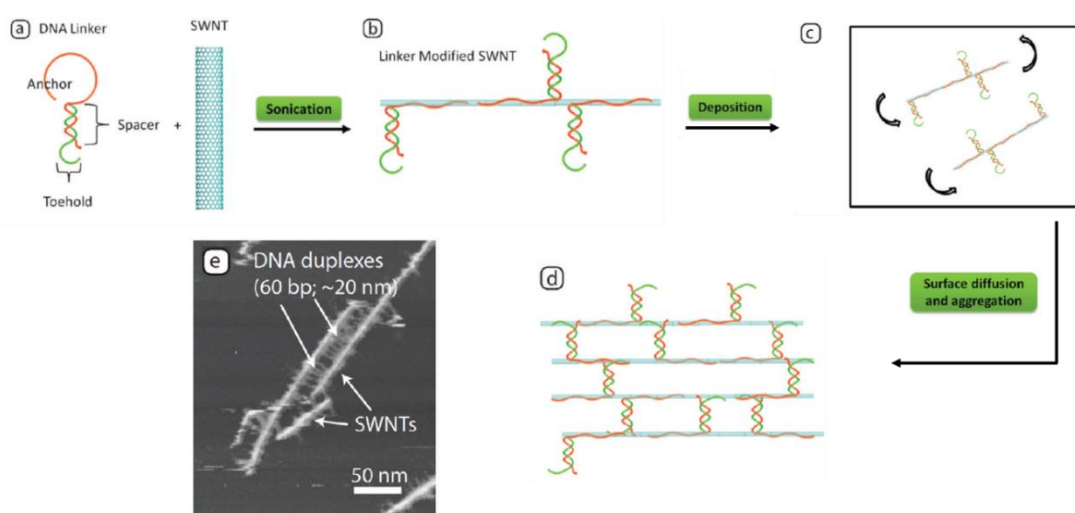


Figure 13. Schematic illustration of linker-induced surface assembly process. (a) DNA linker and SWNT were sonicated to functionalize SWNTs; (b) DNA linker wrapped SWNTs; (c) The deposition of DNA-SWNTs on charged surface and alignment in (d) parallel arrays due to surface diffusion; (e) AFM image of DNA-SWNT arrays with ~22nm pitch on mica surface [70].

In this thesis, a specially designed DNA nanostructure was utilized to build SWNT assemblies in a controllable manner. Prepared DNA-3WJ/SWNT nanohybrids allowed the fluorescence labeling and precise dispersion of SWNTs by utilizing DNA-3WJ for the self-assembly of SWNTs into dendrimer nanostructures. We hypothesized that arrangement of three SWNTs into three-armed DNA junctions might enhance NIR light absorption by 3 times compared to individual SWNTs at the same concentration. This improvement provides a valuable approach for utilization of CNT based nanomaterials as photothermal agents with higher efficiency.

1.4. Thesis Overview

The light-activated heat generation through nanoparticles has attracted much attention for antibacterial and antitumor applications over the last few years. Utilization of these nanoparticles as photothermal agents can provide an effective, alternative solution for the fight against antibiotic resistant bacteria and biofilm formation. However, their heat generation capacity is restricted with the inherent light absorption properties of these nanoparticles. To the extent of our knowledge, no previous studies have addressed to improve their photothermal properties to reach higher light-to-heat conversion efficiencies.

This study focuses on the improvement and characterization of photothermal properties of CNTs to allow the effective conversion of NIR laser light and sunlight into heat. We utilized two methods to improve the light absorption and heat generation capacity of CNTs and develop CNT based photothermal agents which are effective against bacteria. As the first method, we decorated the surface of CNTs with arrays of fluorophores which acted as a light harvesting antenna to increase the amount of light absorbed and the amount of heat generated as a result of the photothermal conversion. The second method is the use of three-armed DNA junctions to organize CNTs into dendrimer nanostructures resulting in improved NIR absorption by 3-fold per hybrid. The methods for preparing CNT/Fluorophore and DNA-3WJ/SWNT nanostructures are summarized in Figure 14.

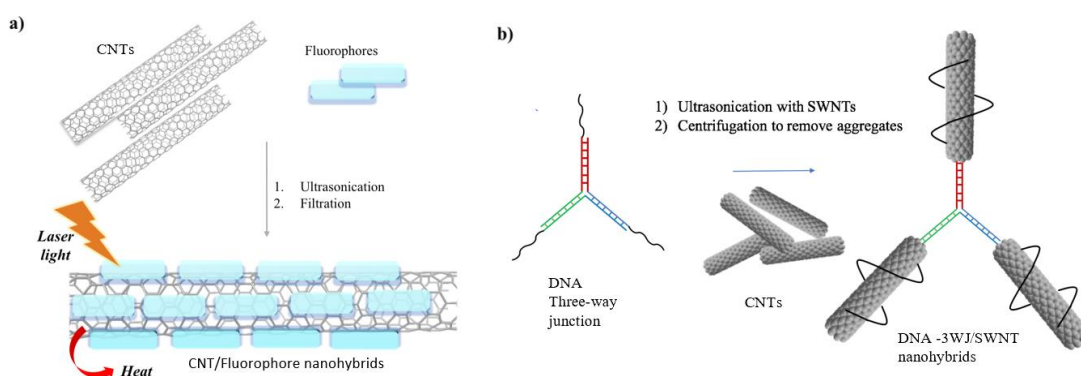


Figure 14. Schematic representation of the preparation of (a) CNT/Fluorophore and (b) DNA-3WJ/SWNT nanostructures.

How arrays of fluorophores self-assembled on CNTs and the change in photophysical properties of CNTs with the nanostructure formation will be discussed. Photophysical characterization of CNT/Fluorophore nanostructures will be followed by testing of their killing efficiencies on bacteria through light activated heat generation. Similarly, the

impact of the assembly of three individual SWNT molecules into a DNA junction on the photothermal properties of resulting nanohybrids will be investigated.

Partial results of this thesis were published as 'DNA directed self-assembly of single walled carbon nanotubes into three-way junction nanostructures' (ACS Omega, 3 (4), 4157-4162) and submitted for publication as 'Fluorophore-decorated carbon nanotubes with enhanced photothermal activity as antimicrobial nanomaterials'.

CHAPTER 2. FLUOROPHORE-DECORATED CARBON NANOTUBES WITH ENHANCED PHOTOTHERMAL ACTIVITY AS ANTIMICROBIAL NANOMATERIALS

2.1. Introduction

Contamination of materials and surfaces with pathogenic bacteria and biofilms constitutes an important challenge in various settings ranging from hospital environments to food processing facilities and necessitates an interdisciplinary research approach for creating solutions. The traditional approach of treating bacteria with biochemical tools such as antibiotics is not a viable option anymore as more bacterial strains have gained resistance to antibiotics [77, 78]. Alternative approaches to deactivate bacteria are needed that do not focus on biochemical pathways, but focus on physically destroying bacteria instead. Photothermal therapy based on nanomaterials that absorb light and release it in the form of heat through non-radiative relaxation provides a promising and effective alternative approach to kill bacteria. Light induced local elevated temperatures generated around photothermal nanomaterials physically destroy bacteria through hyperthermia effects. Inorganic nanoparticles exhibiting localized surface plasmon resonance such as various gold nanostructures demonstrate strong photothermal properties and are widely utilized for killing bacteria [79-83]. Similarly, some near-infrared (NIR) absorbing organic nanoparticles were also demonstrated as efficient photothermal agents [84-87]. Another group of nanoparticles exhibiting photothermal properties due to their NIR light absorption capacities are carbon-based nanoparticles such as carbon nanotubes and graphene [15, 18-21, 88-92]. The fact that carbon nanotubes present inherent binding affinity for bacteria along with their lower costs render them advantageous over gold nanoparticles as photothermal agents for killing bacteria [18]. On the other hand, carbon nanotubes present significantly lower NIR light absorption capacities than gold nanostructures which make them inferior in terms of the NIR light induced temperature elevations they can generate [24]. Thus, enhancing the NIR light absorption capacities of carbon nanotubes can result in excellent photothermal agents which can absorb NIR light with higher capacity and generate higher local temperatures resulting in more effective killing efficiencies on bacteria they spontaneously interact. In this work, we focused on enhancing the NIR light absorption capacity of carbon nanotubes by fluorophores to

obtain photothermal agents that generate high temperature elevations and are effective against bacteria. How fluorophores interact with carbon nanotubes were attractive to researchers in various different aspects. Fluorophores were demonstrated to be useful as carbon nanotube dispersing agents, as electron donor-acceptor systems, as quenchers in carbon nanotube based fluorescent sensors or as fluorescent labels for the visualization of carbon nanotubes [54, 93-100]. Fluorophores can interact with the sp^2 hybridized electronic system of carbon nanotubes through non-covalent interactions such as π - π stacking, Van-der-Waals or hydrophobic interactions resulting in fluorophore/carbon nanotube hybrid structures with different functionalities that are easily tunable. Here we report the decoration of multi walled carbon nanotubes (MWNTs) with fluorophores to enhance their NIR light absorption capacity and photothermal effect where fluorophores act as an antenna to increase the amount of light absorbed and the amount of heat generated as a result of the photothermal conversion. The light harvesting effect originating from fluorophores allows generation of NIR irradiation induced high temperature elevations and bacteria killing rates that could not be reached by irradiation of MWNTs only.

2.2. Experimental

2.2.1. Materials

MWNTs with 13-18 nm outer diameter, 3-30 μm length and 99 wt% purity were provided by Cheap Tubes Inc (Cambridgeport, VT, USA). 3,3'-diethylthiatricarbocyanine iodide (DTTC, 99%) was purchased from Sigma Aldrich (Germany). Triton X-100 was purchased from Merck-Millipore (Darmstadt, Germany). *Pseudomonas aeruginosa* (*P. aeruginosa*, ATTC 27853) were purchased from Medimark (France). Nutrient broth (NB) was purchased from Biolife (Milano, Italia). LIVE/DEAD BacLight Bacterial Viability Kit (L7012) was purchased from Life Technologies (Carlsbad, CA, USA). Centrifugal filter devices (30 kDA cutoff, Microcon) were purchased from Millipore (MA, USA). Anionic, aqueous polyurethane (PU) dispersion based on a polyester-polyol was kindly supplied by Punova R&D and Chemicals Inc. (Turkey) with a 35 wt.% solid content.

2.2.2. Preparation of MWNT and MWNT/DTTC nanohybrids

10 mL of a dispersal solution containing 0.2 mg/mL MWNTs and 20 μM DTTC was sonicated in ice with a microprobe (QSonica, Q700) for 20 min with 4 s pulse on and 5 s pulse off time at a power of 4-5 W. For the preparation of MWNT sample, the same amount of MWNT was dispersed in water containing 5 wt.% Triton X-100 under the same conditions. Aqueous dispersions were centrifuged at 5000 rpm for 5 min to remove MWNTs that are not dispersed. The black colored supernatant was pipetted into a clean falcon tube. Removal of unbound dye molecules was performed using Microcon centrifugal filters according to manufacturer's instructions. Concentration of MWNT and MWNT/DTTC dispersions were determined by absorbance spectroscopy (Cary 5000 Spectrophotometer) using the specific extinction coefficient for MWNTs at 500 nm ($\epsilon_{500} = 46 \text{ mL}\cdot\text{mg}^{-1}\cdot\text{cm}^{-1}$) [101].

2.2.3. Characterization of MWNT/ DTTC nanohybrids

Absorbance spectroscopy was performed to confirm the increase in absorbance capacity after nanohybrid formation. Samples were scanned in a quartz cuvette in the wavelength range of 200 to 1000 nm.

Fluorescence spectra of nanohybrids were obtained with a Cary Eclipse Fluorescence Spectrophotometer. DTTC and MWNT/DTTC were scanned in a quartz cuvette at 720 nm excitation.

2.2.3.1. Laser activated heating in MWNT/DTTC nanohybrids

In order to make an accurate comparison of laser activated heat generation by MWNT and MWNT/DTTC, dispersions of equal MWNT concentrations (0.01 mg/mL) were prepared. 1.2 mL of a DTTC solution (20 μ M) along with MWNT and MWNT/DTTC dispersions were exposed to continuous laser irradiation with a laser power of 1 W/cm² at 808 nm for 15 min. (STEMINC, SMM22808E1200) (Doral, FL USA). Temperature was recorded every three min with a thermocouple (Hanna HI 935005 K-Thermocouple Thermometer). The thermocouple was placed inside the dispersion without blocking the path of the laser beam to avoid the direct heating of the thermocouple by irradiation of laser light.

2.2.3.2. Laser activated antimicrobial activity of MWNT/DTTC hybrids

3 mL overnight cultures of *P. aeruginosa* were grown in NB medium at 37°C in a shaker incubator. Cells were washed twice by centrifugation at 5000 rpm for 5 min and resuspended in sterile phosphate buffered saline (PBS). Bacterial suspensions (2×10^8 CFU/mL) were mixed with dispersions of MWNTs and MWNT/DTTC nanohybrids containing 0.01 mg/mL MWNTs. A control sample containing the same number of bacteria in 1.2 mL of water was also prepared and labeled as 'cells only'. Two sets of 'cells only', '*P. aeruginosa*-MWNT' and '*P. aeruginosa*-MWNT/DTTC' mixtures were prepared to investigate the photothermal destruction of bacteria during laser treatment. While the first set was irradiated with 808 nm NIR laser light for 15 min, the second set was kept in ice. The viability of *P. aeruginosa* in prepared samples before and after laser irradiation was determined by using the Live/Dead viability assay. 0.1 mL of each sample was transferred into a 96-well plate and stained with LIVE/DEAD Baclight kit for 20 min in the dark at room temperature. The ratio of fluorescence intensity of live cells (SYTO 9, ex/em ~ 480/500 nm) to the fluorescence intensity of dead cells (propidium iodide, ex/em ~ 90/635 nm) was calculated for each sample. The fluorescence intensities at 538 and 612 nm were measured with a Fluoroskan Ascent FL microplate reader (Thermo Labsystems). Live/dead cell ratio of the 'cells only' sample that was not irradiated with the laser was specified as 100% cell viability. The viability of each sample was

determined in comparison to this reference sample. Experiments were conducted in triplicates.

2.2.3.3. Scanning Electron Microscopy (SEM)

Following the viability assay, samples composed of *P. aeruginosa* and *P. aeruginosa*-MWNT/DTTC were centrifuged at 14 000 rpm for 5 min and the supernatant was removed. The pellet containing the cells and MWNT/DTTC were fixed in 2.5 % glutaraldehyde in sterile PBS for 2 h at room temperature. The samples were rinsed twice with sterile PBS. Pellets were transferred onto aluminum SEM stubs and air dried. Secondary electron images of samples were obtained with a Zeiss Leo Supra 35 Scanning Electron Microscope.

2.2.4. Preparation of MWNT/DTTC-PU Coatings

MWNT/DTTC-PU nanocomposite coatings were prepared to investigate the photothermal activity of nanohybrids on surfaces. 3 g of aqueous PU dispersion with a solid content of 35% was thoroughly mixed with 2 mL of MWNT and MWNT/DTTC dispersions containing 0.006 mg/mL under overhead agitation and allowed to mix for 1 h, resulting in 0.001 wt. % MWNTs in solid PU. MWNT-PU and MWNT/DTTC-PU dispersions were cast onto petri dishes and dried overnight in an oven at 50°C to evaporate the water content and produce self-standing nanocomposite films. PU film prepared by the same procedure without adding MWNT dispersion was used as a control. Each film was cut into 1 × 1 cm pieces for further experiments.

2.2.4.1. Laser activated heating in MWNT/DTTC-PU coatings

K type cable thermocouple was fixed in place between Teflon plate and a piece of film (1 × 1 cm) for each sample. PU, MWNT-PU and MWNT/DTTC-PU films were exposed to continuous laser irradiation with a laser power of 1 W/cm² at 808 nm for 3 min. Temperature was recorded every 30 s. During the laser irradiation, the thermocouple heated up due to direct absorption of laser light. To correct for this direct heating effect, the maximum temperature reached by the thermocouple itself in the exact same experimental setup was determined and subtracted from each data point when generating the time-temperature curves.

2.2.4.2. Laser activated antibiofilm properties of MWNT/DTTC-PU coatings

After wiping the film surface with ethanol, they were incubated with 2 mL of *P. aeruginosa* suspension containing 2×10^8 CFU/mL in a 12-well plate overnight at 37°C without shaking. The culture medium with nonadherent bacteria was removed and films were gently washed twice with sterile PBS. Films were stained using LIVE/DEAD BacLight kit and incubated for 10 min in the dark at room temperature. The excess staining solution was rinsed with PBS. Films were mounted onto coverslips and examined with a Carl-Zeiss LSM 710 Laser Scanning Confocal Microscope equipped with a Plan-Apochromat 63x/1.40 oil objective before and after exposure to NIR laser light for 15 min. Reported images are 3-D renderings of Z-stacks created by using Zen 2010 Software.

2.3. Results and Discussion

For the enhancement of light absorption capacity of MWNT's in the NIR region, MWNTs were decorated with the NIR-absorbing dye, 3,3'-Diethylthiatricarbocyanine (DTTC). As a symmetrical carbocyanine dye exhibiting strong NIR light absorbing capacity and high resonance Raman cross section DTTC has been widely utilized as fluorescent labels in biomedical imaging and as Raman labels for surface-enhanced Raman spectroscopy [102-106]. Here, DTTC molecules were aimed to build light harvesting arrays on the surface of MWNTs to increase the amount of light absorbed and converted to heat by MWNT/DTTC hybrids. MWNTs were dispersed in an aqueous solution of DTTC through ultrasonication followed by ultracentrifugation to remove aggregated forms of MWNTs that were not dispersed and filtration to remove unbound dye molecules (Figure 15a). Images of resulting MWNT/DTTC hybrids were demonstrated in Figure 15b. While MWNTs were not dispersed in water under the same conditions, they were finely dispersed in an aqueous solution of DTTC molecules as can be seen by the darker color of resulting stable mixtures. DTTC molecules acted as strong dispersing agents that debundled MWNTs potentially due to strong noncovalent interactions such as π - π stacking and Van der Waals interactions resulting in MWNTs decorated with dye molecules.

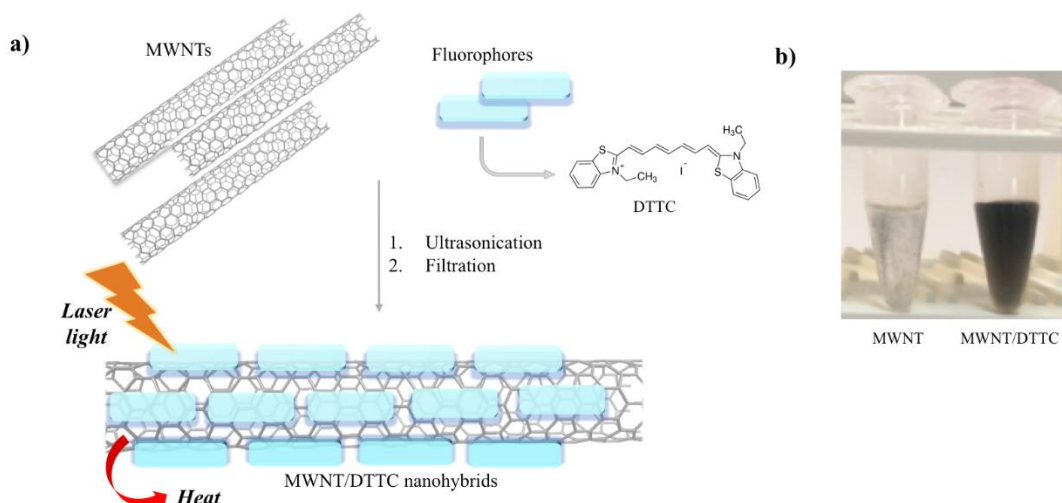


Figure 15. a) Schematic demonstrating the preparation of MWNT/DTTC nanohybrids. b) photographs of MWNTs sonicated in water (left) and in an aqueous solution of DTTC (right).

Non-covalent binding interactions between MWNTs and DTTC molecules were characterized by absorption spectroscopy. The normalized absorption spectrum of free DTTC molecules in aqueous solution was compared to the normalized absorption spectrum of MWNT/DTTC hybrids to comment on the binding interactions that are formed (Figure 16a). The absorption spectrum of MWNT/DTTC hybrids demonstrated a bathochromic shift of 50 nm relative to free DTTC molecules indicating a significant change in the electronic environment which confirms non-covalent binding of DTTC molecules onto MWNTs. Previous studies on aggregates of dyes suggest that a bathochromic shift usually indicates a J-aggregate where dye molecules form an edge-to-edge array on a template. The fact that the absorption spectrum of DTTC molecules presented a similar shift implies that DTTC molecules form an array on MWNTs resulting in MWNTs decorated with fluorophores. The effect of dye molecules on MWNT spectrum was also investigated. Figure 16b demonstrates the absorption spectrum of MWNT/DTTC hybrids in the NIR region in comparison to MWNTs dispersed in a surfactant solution. MWNT/DTTC hybrids demonstrate an additional absorption peak that is not present in the absorbance spectrum of MWNTs, indicating that the presence of DTTC molecules have enhanced the absorption capacity of MWNTs in the NIR region. As more of NIR light can be absorbed by MWNT/DTTC hybrids, they can potentially convert more of the light energy to heat energy resulting in higher temperature elevations when irradiated with a NIR laser.

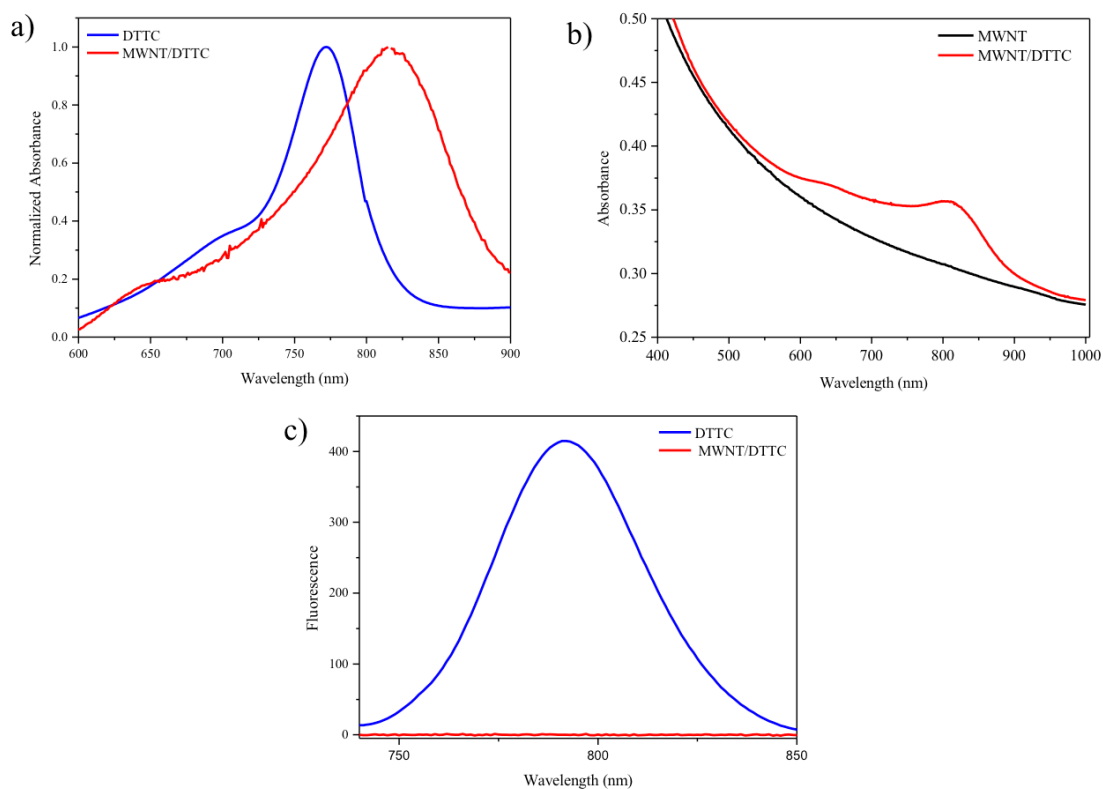


Figure 16. a) Normalized absorbance spectra of DTTC and MWNT/DTTC containing equal concentrations of DTTC. b) Absorbance spectra of MWNTs and MWNT/DTTC containing equal concentrations of MWNTs. c) Fluorescence spectra of DTTC and MWNT/DTTC containing equal concentrations of DTTC.

NIR Fluorescence spectra of prepared hybrids were also investigated in order to comment on the conversion of the absorbed light energy into different forms of energy. Fluorescence emission of DTTC molecules centered around 800 nm was completely quenched when they form hybrids with MWNTs; hybrids did not emit fluorescence light (Figure 16c). This result indicates that all the light energy absorbed by MWNT/DTTC hybrids was converted into heat energy, which makes these hybrids potential photothermal agents.

Photothermal properties of MWNT/DTTC hybrids were studied by measuring their NIR laser activated temperature elevations. Dispersions of MWNTs and MWNT/DTTC hybrids were irradiated with 808 nm laser for 15 minutes while their temperatures were monitored. While the dispersion of MWNTs reached only 69°C after 15 minutes of irradiation, MWNT/DTTC hybrids demonstrated an extra 22°C temperature elevation and reached 92°C (Figure 17a). The array of DTTC molecules self-assembled on the

surface of MWNTs enhanced the amount of NIR light absorbed; thus, the amount of energy converted into heat and caused significantly larger temperature elevations. The temperature of a solution of free DTTC molecules did not present a significant temperature elevation when irradiated with NIR laser light under the same conditions confirming that large temperature elevations demonstrated by MWNT/DTTC hybrids are actually caused by the photothermal effect of hybrids and not by direct heating by the laser.

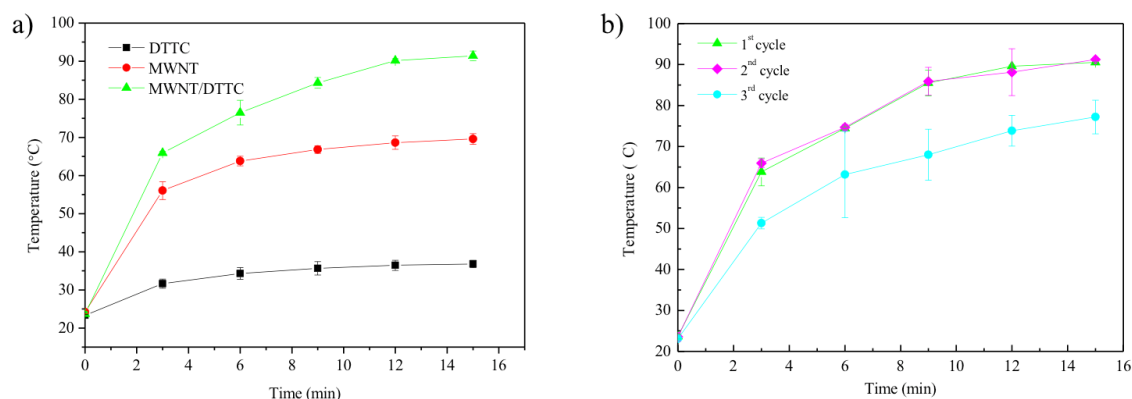


Figure 17. a) Time-temperature curves of DTTC, MWNT and MWNT/DTTC containing equal DTTC and MWNT concentrations generated by 808 nm NIR laser irradiation for 15 min. b) Time-temperature curves generated by 808 nm NIR laser irradiation of the same MWNT/DTTC nanohybrid sample for three consequent cycles.

The potential of MWNT/DTTC hybrids as multiple-use photothermal agents was also studied. Figure 17b presents heating curves obtained when MWNT/DTTC hybrids that were already irradiated for 15 minutes with laser light were irradiated again for the second and third time. At the end of the second cycle of irradiation MWNT/DTTC hybrids were able to reach the same temperature they reached in the first cycle. This result demonstrates that MWNT/DTTC hybrids remained stable at high temperatures; the array of DTTC molecules on MWNTs did not dissociate. When the hybrids were irradiated with laser light for the third time, the monitored temperature was only 70°C, the same temperature monitored when MWNTs were irradiated for 15 minutes, indicating that DTTC molecules have dissociated from the MWNT template. Results obtained from this experiment show that MWNT/DTTC hybrids can be utilized at least in two rounds of laser irradiation to

generate temperatures reaching 91°C. Rounds of irradiations exceeding two still cause temperature elevations, but temperature elevations are lower than previous rounds.

The photothermal effect of MWNT/DTTC hybrids was demonstrated as their ability to kill bacteria. Laser-activated antimicrobial properties of MWNT/DTTC hybrids were tested on *P. aeruginosa* as a gram-negative model microorganism. *P. aeruginosa* treated with MWNT and MWNT/DTTC dispersions of equal concentrations along with *P. aeruginosa* that are not treated were irradiated with NIR laser for 15 minutes. Viabilities of cells before and after laser irradiation were determined by live-dead staining where *P. aeruginosa* cells sample before laser treatment was designated as the reference for 100% viability (Figure 18). MWNTs presented antibacterial activity on *P. aeruginosa* even before the laser treatment as can be seen by the lower viability value compared to cells that are not treated with MWNTs. Such antimicrobial effect of MWNTs due to their noncovalent interactions with bacterial cell walls was demonstrated before. MWNT/DTTC hybrids, on the other hand, did not present antimicrobial activity on *P. aeruginosa* cells before the laser treatment. Probably, the array of DTTC molecules formed on the surface of MWNTs prevents interactions of MWNTs with cells and shield the toxic effect. Viability of bacteria treated with MWNTs and MWNT/DTTC hybrids after NIR laser treatment demonstrated the photothermal effect of these nanostructures. When not treated with MWNTs or MWNT/DTTC hybrids, *P. aeruginosa* were not killed by the laser irradiation under the same conditions confirming that the laser irradiation itself does not present any toxic effect on bacteria. When MWNTs in the bacterial suspension were irradiated with NIR laser light for 15 minutes, they killed 52% of *P. aeruginosa* cells in the suspension due to their inherent photothermal effect. On the other hand, when *P. aeruginosa* treated with MWNT/DTTC hybrids were irradiated with NIR laser light, the killing efficiency was 77% indicating that MWNTs decorated with DTTC molecules presented enhanced photothermal effect resulting in significantly stronger laser activated antimicrobial activity than MWNTs only. The local high temperatures generated by MWNT/DTTC hybrids resulted in physical damage that a majority of cells were not able to survive. The enhanced absorption capacity of MWNT/DTTC hybrids enabled by the array of DTTC molecules formed on MWNTs resulted in larger laser light activated temperature elevations and larger antimicrobial activity.

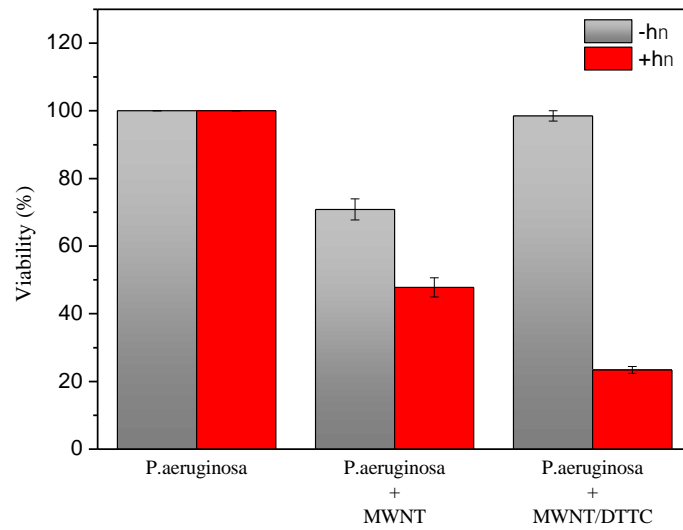


Figure 18. Viability of *P. aeruginosa* cells in the presence and absence of MWNTs and MWNT/DTTC nanohybrids before and after 808 nm laser irradiation for 15 min.

Physical destruction of bacteria through heat generated by MWNT/DTTC hybrids after laser treatment is also demonstrated by SEM. Figure 19 presents *P. aeruginosa* cells alone and *P. aeruginosa* cells treated with MWNT/DTTC hybrids before and after NIR laser treatment. The control sample including cells only did not exhibit any structural deformation after laser treatment, confirming that the direct absorption of NIR laser light does not present any toxicity on cells. When cells are treated with MWNT/DTTC hybrids followed by laser irradiation for 15 minutes, they presented deformed structures where outlines of cells mostly disappeared. Extensive temperature elevations caused by the MWNT/DTTC hybrids lead to lysis of cell walls potentially due to heat activated protein denaturation.

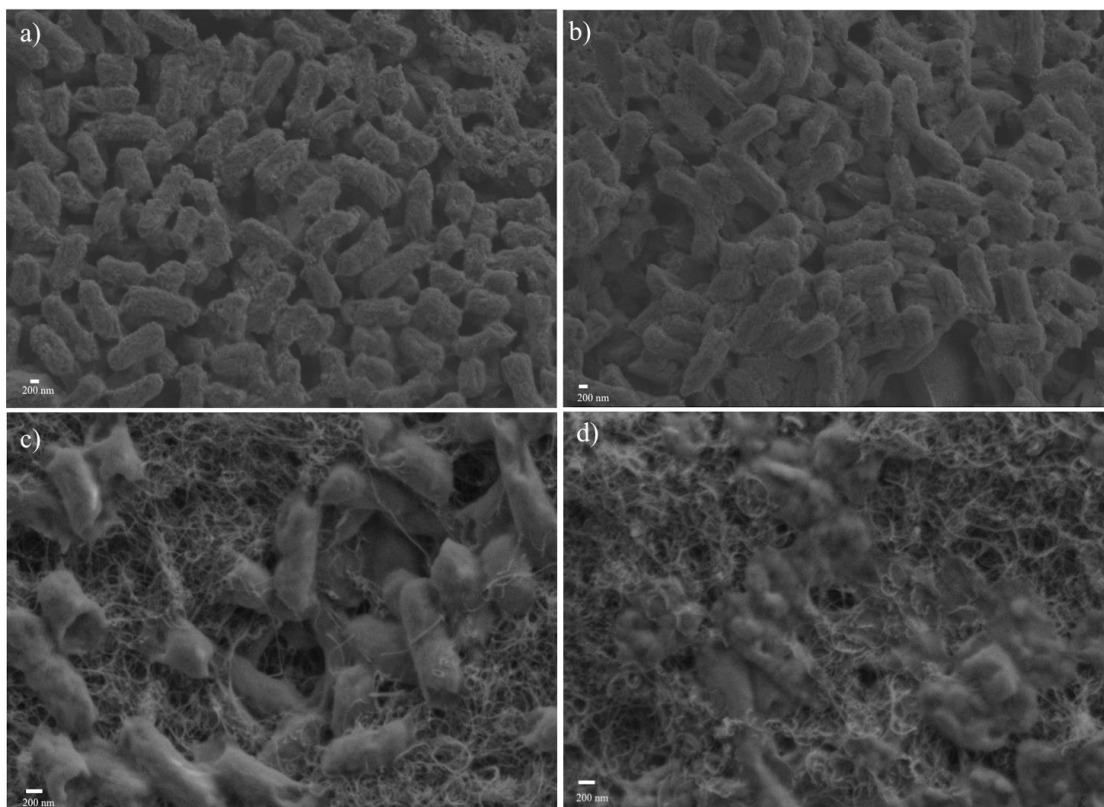


Figure 19. Representative SEM images of *P. aeruginosa* cells alone (a, b) and *P. aeruginosa* cells in the presence of MWNT/DTTC nanohybrids (c, d). Images a and c were obtained before 808 nm laser irradiation; images b and d were obtained after 808 nm laser irradiation.

MWNT/DTTC hybrids exhibiting strong light activated antimicrobial activity were incorporated into water-based polyurethane (PU) coating materials in order to evaluate their activity on surfaces as antimicrobial and antibiofilm coatings that can kill attached bacteria upon NIR laser irradiation (Figure 20). Aqueous PU dispersions composed of polyester-based PU were blended with MWNTs and MWNT/DTTC nanohybrids resulting in nanocomposites containing 0.001 wt.% MWNTs homogeneously distributed within the PU matrix. Photothermal activity of MWNT/DTTC-PU nanocomposites were demonstrated on self-standing cast films demonstrated in Figure 20 (inset).

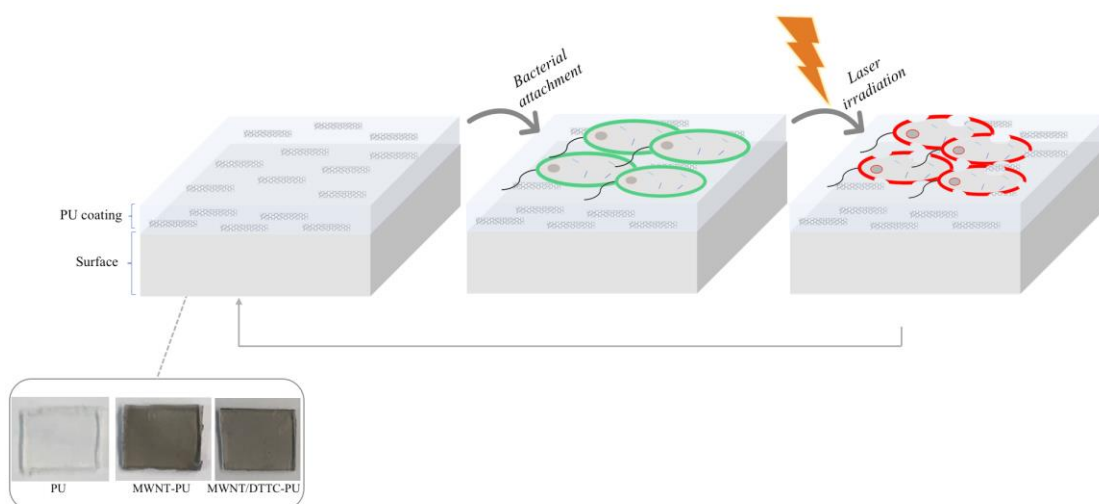


Figure 20. Schematic demonstrating the application of MWNT/DTTC-PU nanocomposites as antimicrobial surface coatings. Inset: Photographs of PU, MWNT-PU and MWNT/DTTC-PU nanocomposites as self-standing films.

The photothermal activity of MWNT-PU and MWNT/DTTC-PU nanocomposite films were determined by measuring temperatures generated upon NIR laser irradiation. Figure 21 demonstrates that the temperature of MWNT/DTTC-PU film was quickly raised up to 120°C within two minutes. While the MWNT-PU film was also heated up within the same period of laser irradiation, it presented a 30°C lower temperature indicating that the presence of DTTC dye array around MWNTs significantly increases their photothermal effect even when embedded within a polymer matrix. The PU film without MWNTs did not present an increase in temperature confirming that elevated temperatures were caused by the photothermal activity of MWNTs and MWNT/DTTC hybrids. MWNT/DTTC nanohybrids embedded within the PU matrix generated much higher temperatures than the same amount of MWNT/DTTC nanohybrids in aqueous dispersion, potentially because of the lower heat conductivity of the polymeric material that locks in the heat. High temperatures generated by these coating materials make them excellent candidates for antimicrobial surfaces as these temperatures would be toxic to most of bacterial species. The potential of MWNT/DTTC-PU nanocomposites as reusable surface coatings retaining photothermal activity post laser treatment was also investigated (Figure 21b). When MWNT/DTTC-PU films already irradiated with laser for 3 min were irradiated again for the second and third time, they reached the same elevated temperature of 120°C

as in the first cycle indicating that these materials can be applied onto surfaces where bacterial attachment will reoccur and bacterial inactivation will be needed multiple times.

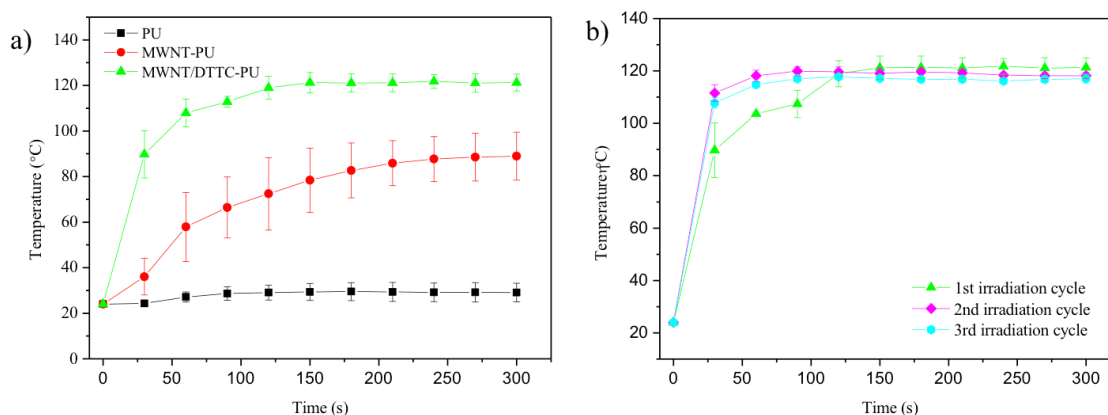


Figure 21. a) Time-temperature curves of PU, MWNT-PU and MWNT/DTTC-PU films generated by 808 nm NIR laser irradiation for 5 min. b) Time-temperature curves generated by 808 nm NIR laser irradiation of the same MWNT/DTTC-PU film for three consequent cycles.

The laser-activated antimicrobial activity of MWNT/DTTC-PU coating materials was demonstrated as their ability to kill surface attached bacteria upon NIR laser irradiation. MWNT/DTTC-PU films were incubated with *P. aeruginosa* overnight in static growth conditions for 24 h to allow adhesion of bacteria onto film surfaces followed by staining with live/dead cell indicator dyes. Stained surfaces were imaged with laser scanning confocal microscopy before and after NIR laser irradiation for 15 min. Representative images are shown in Figure 22. While bacteria attached to the PU surface remained alive following the NIR laser irradiation for 15 min, all bacteria attached to the MWNT/DTTC-PU surface died following the laser treatment. The high temperatures generated by the MWNT/DTTC-PU surface during the laser irradiation physically damaged and killed attached bacteria demonstrating the potential of these surfaces as antibiofilm surfaces that can eradicate established biofilms.

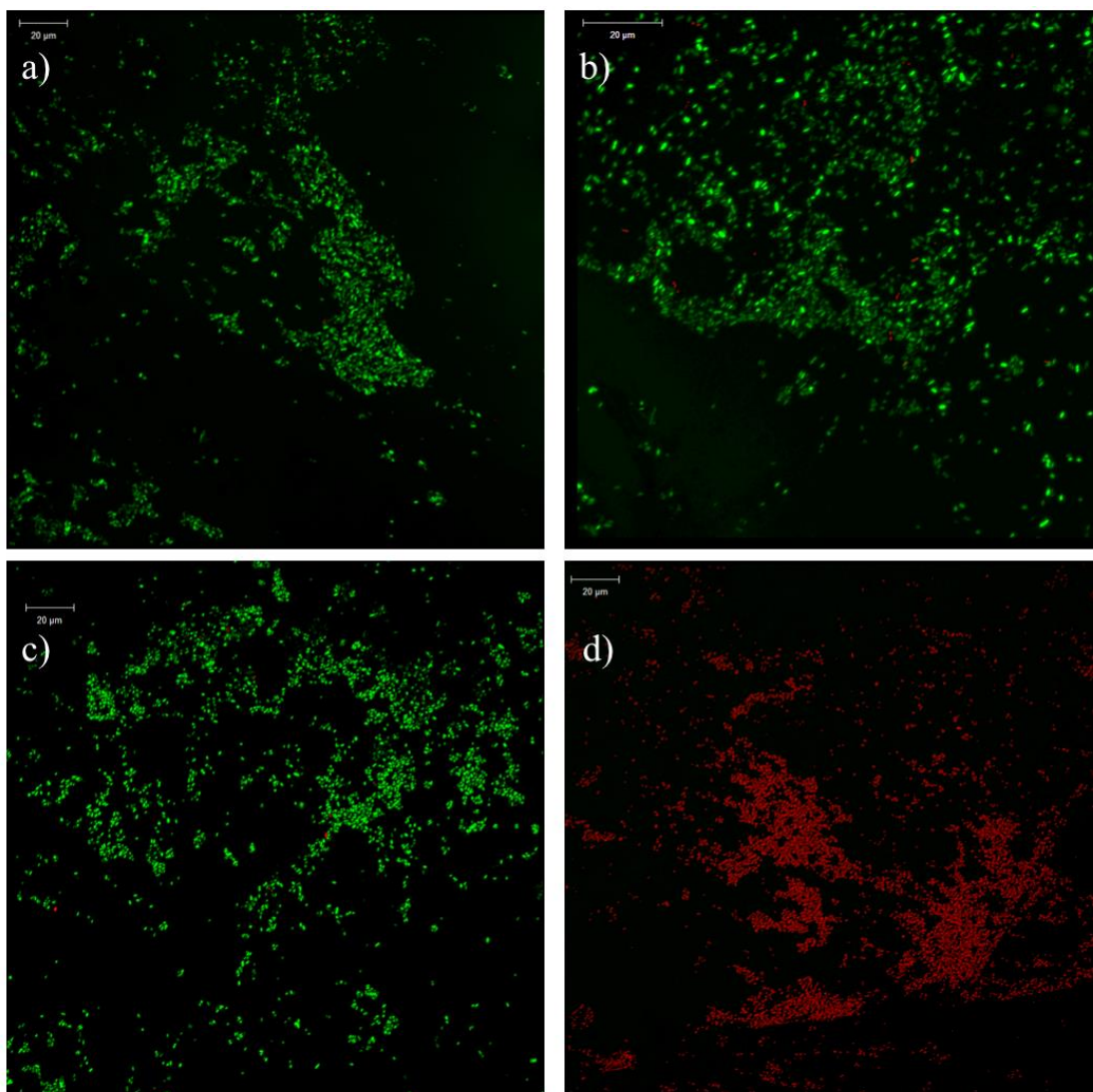


Figure 22. Representative laser scanning confocal microscopy images of PU (a,b) and MWNT/DTTC-PU surfaces (c,d). Images a and c were obtained before 808 nm laser irradiation; images b and d were obtained after 808 nm laser irradiation.

CHAPTER 3. DNA DIRECTED SELF-ASSEMBLY OF SINGLE WALLED CARBON NANOTUBES INTO THREE-WAY JUNCTION NANOSTRUCTURES

3.1. Introduction

SWNTs are essential building blocks for the fabrication of nanoscale devices with potential applications in electronics, optics and biosensing. The main challenge in the utilization of remarkable thermal, electrical and electronical properties of SWNTs in such nanoscale devices is to precisely control the assembly of SWNTs into desired nanoarchitectures. The ability to direct the positioning of SWNTs at the nanoscale could allow the creation of macroscopic assemblies that parallel the distinct properties of individual nanotubes. Several studies focused on building SWNT junctions as-synthesized on surfaces and in solution using post-synthesis methodologies [107-117]. A promising approach to build controllable SWNT assemblies is the utilization of single stranded DNA (ssDNA) as information-containing biomolecules. ssDNA is a useful tool for materials chemistry as it can be programmed into complex nanostructures through hybridization and allows both covalent and noncovalent functionalization to build hybrid materials [118, 119]. The fact that ssDNA can form strong π - π interactions with SWNTs resulting in helical wrapping, makes it a useful agent that can be utilized for SWNT dispersion, sorting and labelling [120]. Hybrids of ssDNA and SWNTs can be prepared where the ssDNA can act as both the dispersing agent by wrapping the SWNT and also as the linker molecule that joins SWNTs wrapped with ssDNA of complimentary sequences through hybridization. The ability of ssDNA to direct the self-assembly of SWNTs into controlled aggregates or two-dimensional complex geometries in solution or on ssDNA immobilized surfaces has been demonstrated in a limited number of studies [69, 121-127]. On the other hand, a facile method to arrange SWNTs into controlled nanostructures utilizing pre-assembled DNA nanostructures that link the self-assembly of SWNTS through in-solution, noncovalent interactions is missing.

Here we demonstrate the utilization of a specially designed ssDNA 3WJ nanostructure to build branched SWNT building blocks in solution. Ghosh et. al. demonstrated the positive impact of DNA-encasement of MWNTs on obtaining the stable dispersion, and enhanced

heat generation when irradiated with NIR laser light (referans ekle!). They utilized this light-induced temperature elevation generated by DNA-encased MWNTs for thermal ablation of cancer cell in vivo. Similarly, our novel approach provides a straightforward method to design CNT based photothermal agents with high NIR light absorption capacity. DNA-3WJ nanostructures possessing linker sequences available for wrapping the SWNT allow the self-assembly of three individual SWCNTs into a Y-junction. Depending on the route of preparation, these SWNT Y-junctions can act as building blocks for the formation of larger networks of SWNTs as well. Prepared DNA-3WJ/SWNT nanohybrids demonstrated an increase in the amount of NIR light absorbed with the self-assembly of three SWNTs into dendrimer nanostructures, which induced higher local temperature elevation compared to individual SWNTs.

3.2. Experimental

3.2.1. Materials

Table 1 Sequences of ssDNA utilized for the self-assembly of DNA-3WJ

ssDNA	Sequence	Base number
ssDNA1	GGG GGG GGG GGG GCA GGT GGC GAG AGC GAC GAT CCA T	37
ssDNA2	GGG GGG GGG GGG GAT GGA TCG TCG CAG AGT TGA CCG G	37
ssDNA3	GGG GGG GGG GGG GCC GGT CAA CTC TTC TCG CCA CCT G	37

The powder form of SWNTs with 1-2 nm diameters, 500 nm length and 60% purity were purchased from Nanostructured and Amorphous Materials Inc. in Los Alamos, New Mexico, USA. ssDNA strands to prepare DNA-3WJ nanostructures were synthesized by Sentromer DNA Technologies, Istanbul, Turkey. The sequences of ssDNA used in this study are listed in Table 1. Asymmetrical cyanine dye, YOYO-1 (Y3601), was purchased from Life Technologies. The gel was stained with GelRed by Biotium, USA. DNA-3WJ/SWCNT nanohybrids were filtered with Amicon Ultra 0.5 mL Centrifugal Filters with 30k membrane cut-off by EMD Millipore, Darmstadt, Germany.

3.2.2. Preparation and characterization of DNA-3WJ

To prepare the DNA-3WJ nanostructure, an aqueous solution containing 1 μ M of each ssDNA1, ssDNA2 and ssDNA3 in a buffer (100 mM NaCl, 10 mM Tris and 0.1 mM EDTA) was prepared and annealed by heating to 95° C for 5 minutes and cooling in ice bath.

Visualization of the formation of DNA-3WJ was performed by agarose gel electrophoresis. 12.5 μ L of samples mixed with 2.5 μ L 6X glycerol loading dye, were loaded into a 1% agarose gel pre-stained with GelRed nucleic acid stain. The gel was run

in 1X TBE buffer (89 mM tris(hydroxymethyl)aminomethane, 89 mM boric acid and 2mM EDTA in distilled water). Biorad Gel Doc EZ system was used to visualize the gel. The titration experiment to confirm the formation of DNA-3WJ was conducted on a Cary Eclipse Fluorescence Spectrophotometer. Aliquots of 50 μ M YOYO-1 solution were titrated into a solution containing 0.25 μ M DNA-3WJ. The intensity at fluorescence maximum (510nm) was monitored at increasing YOYO-1 concentrations and the saturation of DNA -3WJ with fluorophores was reached when the intensity levels off.

3.2.3. Preparation of DNA-3WJ/SWNT nanohybrids

To prepare 3WJ-DNA/SWNT nanohybrids with the pre-annealing method, a dispersal solution composed of 0.1 mg mL⁻¹ SWNT and 1 μ M annealed DNA-3WJ was prepared and sonicated with a microprobe (QSonica, Q700) for 30 minutes at a power of 5W with 4 s pulse on and 4 s pulse off time in ice. The dispersion was centrifuged at 14000 rpm for 5 minutes. The black colored supernatant was removed into a clean Eppendorf tube. To prepare 3WJ-SWNT nanohybrids with the post-annealing method, each ssDNA was sonicated with SWNTs separately. 0.5 mL of a solution containing 0.1 mg mL⁻¹ CNTs and 1 μ M of each ssDNA in water was sonicated for 30 minutes with 4 s pulse on and 4 s pulse off time in ice. Following the sonication, equal volumes of all dispersion solutions were mixed and annealed by heating to 95° C for 5 minutes and cooling in an ice bath. The dispersion was centrifuged to remove the unbound SWNTs at 14000 rpm for 5 minutes and the supernatant was taken into a clean Eppendorf tube. Any unbound ssDNA was removed using Amicon Ultra filter devices by following the instructions of the filter device.

3.2.4. Characterization of 3WJ-DNA/SWNT nanohybrids

3.2.4.1. Atomic Force Microscopy (AFM)

The supramolecular assemblies of DNA-3WJ/SWNT nanohybrids were characterized by Atomic Force Microscopy in dynamic mode (ezAFM, Nanomagetics Instruments). To perform the experiment on atomically flat surface, the mica sheet was cleaved with the scotch tape a few times. Samples were diluted 1:10 with deionized water. 20 μ L of nanohybrids were deposited onto the freshly cleaved mica sheet for 15 minutes at room temperature. Following the deposition, the surface was rinsed with deionized water and air dried.

3.2.4.2. Scanning Electron Microscopy (SEM)

DNA-3WJ/SWNT nanohybrids were analyzed with a Zeiss Leo Supra 35 Scanning Electron Microscope, using a secondary electron detector. Nanohybrids were diluted 1:10 and 1:200 with distilled water for pre-annealed and post-annealed samples, respectively. 10 μL of nanohybrids were dropped onto an aluminum SEM stub and then air dried for two hours. DNA-3WJ/SWCNT nanohybrids prepared with the pre-annealing method were visualized at accelerating voltage of 4 kV and a working distance of 6 mm. DNA-3WJ/SWCNT nanohybrids prepared with the post-annealing method were visualized at accelerating voltage of 3 kV and a working distance of 7 mm.

3.2.4.3. Agarose gel electrophoresis

Visualization of the mobility of DNA-3WJ/SWNT nanohybrids was performed by agarose gel electrophoresis. 12.5 μL of samples mixed with 2.5 μL of 1:3 glycerol: water solution, were loaded into a 1% agarose gel and the gel was run in 1X TBE. The gel was photographed without any staining.

3.2.4.4. Fluorescence Spectroscopy

Fluorescence spectrum of 3WJ-DNA/SWNT saturated with YOYO-1 was obtained by performing a titration experiment. Aliquots of a 10 μM YOYO-1 solution were titrated into a solution containing 0.25 μM 3WJ-DNA/SWNT. The intensity at fluorescence maximum (510 nm) was monitored at increasing YOYO-1 concentrations and the saturation of the nanohybrid with fluorophores was reached when the intensity levels off.

3.2.4.5. Dynamic Light Scattering (DLS)

Samples were analyzed in a quartz cuvette at 25 $^{\circ}\text{C}$. Nanohybrids were diluted 1:200 with distilled water for measurements. The particle size analysis was performed for 10 cycles with 3 measurements that were used to determine the mean particle size.

3.2.4.6. Laser activated heating in DNA-3WJ/SWNT nanohybrids

Stable dispersions of SWNT and DNA-3WJ/SWNT nanohybrids with equal CNT concentration (0,003 mg/mL) were prepared to reveal the effect of hybrid formation on laser activated heat generation. 0.5 mL of SWNT and DNA-3WJ/SWNT dispersions were exposed to continuous laser irradiation with a laser power of 1 W/cm^2 at 808 nm for 15 min (STEMINC, SMM22808E1200) (Doral, FL USA). Temperature was recorded every three min with a thermocouple placed inside the dispersion without blocking the path of the laser beam (Hanna HI 935005 K-Thermocouple Thermometer).

3.3. Results and Discussion

3.3.1. Preparation and characterization of 3WJ-DNA Nanostructures

The DNA nanostructure utilized to link three individual SWNT molecules into a Y-junction with a controlled angle through noncovalent binding interactions is a DNA-3WJ. The 3WJ is formed by the self-assembly of three ssDNA strands with partially complementary sequences through annealing resulting in a nanostructure with three arms consisting of double stranded DNA and non-complementary overhang sequences for wrapping the SWNT (Figure 23a). The overhang is designed to be a poly-G sequence consisting of 13 guanines which was previously demonstrated to show a strong affinity towards wrapping SWNTs [128]. The successful assembly of the 3WJ was demonstrated with agarose gel electrophoresis (Figure 23b). When all three ssDNA strands were annealed, the corresponding band migrates slower than bands corresponding to individual strands and to the products obtained from annealing two of the ssDNA strands using the same conditions. This result demonstrated the successful formation of the DNA-3WJ nanostructure which migrates slower than control products due to its larger molecular weight.

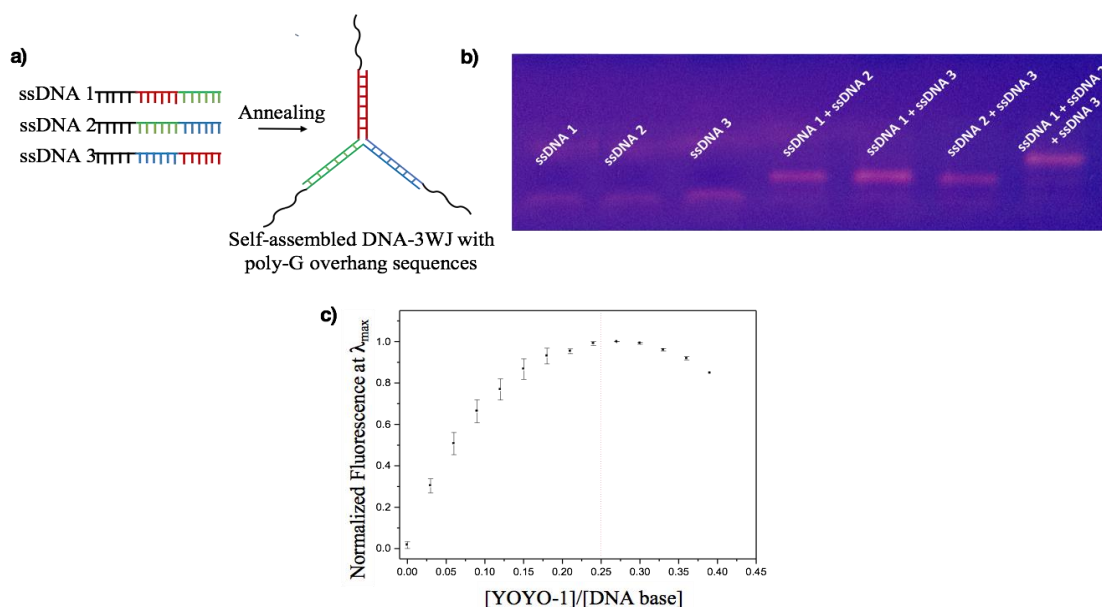


Figure 23. a) Schematic of the self-assembly of DNA-3WJ. Same color regions represent complementary sequences and black regions represent poly-G sequences b) Visualization of the agarose gel loaded with individual ssDNA strands, binary combinations of ssDNA strands and a mixture of all three ssDNA strands. All samples were annealed to 95°C for 5 min and cooled in ice bath c) Fluorescence titration curve demonstrating the increase in fluorescence intensity of DNA-3WJ at increasing fluorophore concentrations.

The formation of the 3WJ nanostructure exactly as designed was further confirmed by measuring the number of base pairs formed by conducting fluorophore-titration experiments. Aliquots of an asymmetrical cyanine dimer, YOYO-1, that is known to bind to DNA base pairs at a ratio of 1:4 was titrated into a DNA-3WJ solution of known concentration and the increase in fluorescence was monitored at increasing fluorophore concentrations. Figure 23c shows that the fluorescence intensity increased with increasing fluorophore concentration as YOYO-1 molecules intercalate between the base pairs of 3WJ and light-up. At a certain point the fluorescence intensity levels off indicating that all binding sites on the nanostructure were saturated with the fluorophore. The fact that this saturation occurred when the ratio of YOYO-1 concentration to the theoretical number of base pairs is 0.25, as expected, confirmed the formation of the 3WJ nanostructure as designed.

3.3.2. Preparation and characterization of hybrids of DNA-3WJ and SWNTs

To assemble SWNTs into 3WJ nanostructures they were ultrasonicated in an aqueous solution of the prepared DNA-3WJ followed by ultracentrifugation to remove any residues that are not dispersed (Figure 24a). While SWNTs of the same concentration were not dispersed in water using the same ultrasonication conditions, SWNTs ultrasonicated in DNA-3WJ solution were finely dispersed indicating that SWNTs were non-covalently interacting with the DNA-3WJ leading to the formation of a hybrid nanostructure (Figure 24b). A control experiment to confirm that DNA-3WJ nanostructures survived the high energy ultrasonication process, agarose gel migration of samples before and after the ultrasonication were compared and shown to have the same mobility demonstrating that the DNA-3WJ template stays intact during the ultrasonication of SWNTs with DNA (data not shown).

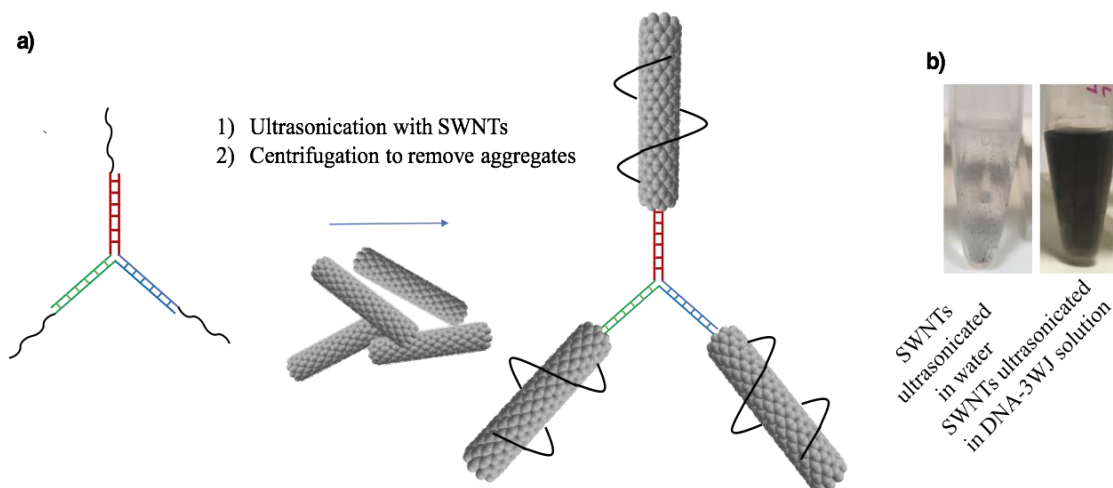


Figure 24. a) Schematic representation of the formation of DNA-3WJ/SWNT hybrid nanostructures b) Photographs of SWNTs ultrasonicated in water (left) and SWNTs ultrasonicated in DNA-3WJ solution.

The formation of DNA-3WJ/SWNT hybrid structures were further characterized with Atomic Force Microscopy (AFM) and Scanning Electron Microscopy (SEM) to confirm that SWNTs are assembled into junctions with a controlled angle. Figure 25a shows representative AFM images of DNA-3WJ/SWNT hybrids. As seen on the images, the DNA-3WJ template guided the assembly of three individual SWNT molecules into one hybrid nanostructure leading to three-armed SWNTs where the angle at their junction point is approximately 120° . The fact that the DNA-3WJ nanostructure is composed of three partially complementary strands that form double stranded DNA arms makes it a rigid template that controls the angle at which the carbon nanotubes join and form the hybrid three-armed SWNT nanostructure. While Y-Junctions of SWNTs were visible on the representative AFM image, individual SWNTs were present as well, indicating that not all SWNTs were able to self-assemble into DNA-3WJ/SWNT nanostructures. We believe that manipulation of DNA-3WJ and SWNT concentrations along with sonication and annealing conditions can improve the yield of DNA-3WJ/SWNT formation. Similar to AFM images, DNA-3WJ templated branched SWNT nanostructures were also visible on SEM images (Figure 25b). Microscopy images obtained confirmed that the design and method applied in this work allowed the DNA-3WJ templated assembly of SWNTs into three-armed junctions.

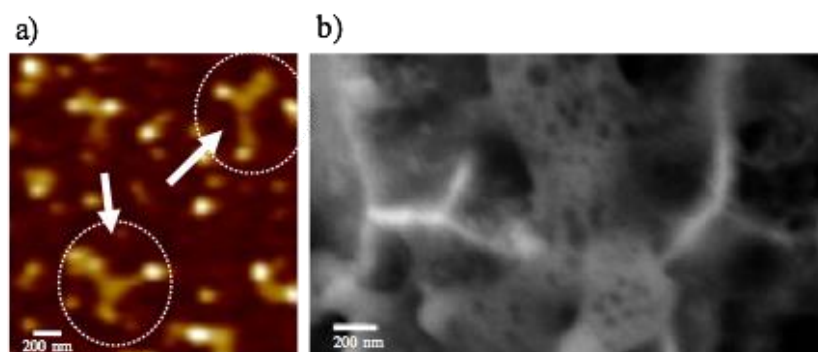


Figure 25. a) AFM topographical image of DNA-3WJ/SWNT hybrid nanostructures, b) Cross sectional analysis of representative topographical AFM (a) and SEM (b) images of DNA-3WJ/SWNT hybrid nanostructures.

DNA-3WJ nanostructures not only acted as templates that facilitate the self-assembly of SWNTs into junctions, they were also shown to provide a relatively better dispersion quality compared to linear ssDNA strands that form the DNA-3WJ. We utilized agarose gel electrophoresis to demonstrate the relative dispersion qualities of SWNT samples as improved quality of dispersion of SWNTs will decrease the particle size and make it easier for SWNTs to enter the gel and migrate. Figure 26a shows a comparison of migration of ssDNA3/SWNT and 3WJ/SWNT hybrids in an agarose gel. While both hybrids entered the gel, 3WJ/SWNT hybrids migrated significantly faster than ssDNA/SWNT hybrids on the agarose gel indicating that SWNTs were dispersed into smaller particle sizes in the DNA-3WJ solution than the linear ssDNA. Dynamic light scattering (DLS) characterization of both samples reporting the average hydrodynamic diameter of SWNTs further confirmed that 3WJ nanostructures provided better dispersion quality compared to a linear ssDNA (Figure 26b). The particle size of SWNTs dispersed using the DNA 3WJ were measured significantly smaller than the particle size of the same amount of SWNT dispersed using a linear equivalent, one of the ssDNA strands forming the DNA-3WJ. Apparently the dendrimeric form of the DNA-3WJ binding sites which allows one DNA-3WJ molecule to wrap three individual SWNT molecules increases the dispersion efficiency.

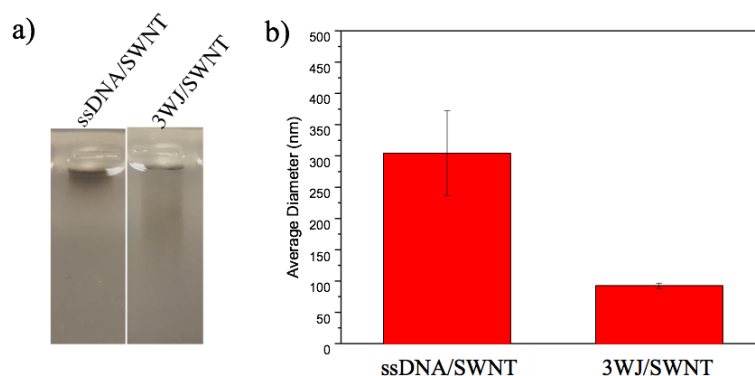


Figure 26. a) Visualization of an agarose gel loaded with equal amounts of ssDNA/SWNT (left) and DNA-3WJ/SWNT (right) b) Average hydrodynamic diameters of ssDNA/SWNT and DNA-3WJ/SWNT hybrids measured by DLS.

We further characterized DNA-3WJ/SWNT nanostructures for their potential for being fluorescently labelled. Fluorescent labelling of nanoparticles provides a great variety of opportunities for the utilization of nanoparticles in biological and sensing applications. Fluorescent labeling of SWNTs with fluorophores has been of particular interest since the inherent fluorescence emission of SWNTs is of very low efficiency and is limited to the NIR region of the spectrum. The main obstacle that limits the fluorescent labeling of SWNTs with fluorophores is the fact that fluorophores in close proximity to SWNT surface are mostly quenched as SWNTs act as electron and energy acceptors [129, 130]. The design of DNA-3WJ/SWNT nanohybrids reported here allows the labelling of the core DNA-3WJ with fluorophores which results in indirect labelling of SWNTs. To investigate whether DNA-3WJ/SWNTs can be labelled with fluorophores, we chose an asymmetric cyanine dye, YOYO-1 which lights up when it intercalates between base pairs of double stranded DNA. Figure 27 shows the fluorescence spectrum of a solution of DNA-3WJ/SWNTs to which a saturating amount of YOYO-1 was added.

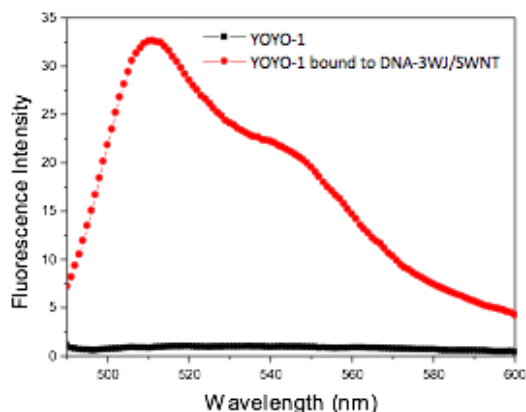


Figure 27. Fluorescence spectra of equal amounts of YOYO-1 i) in water (black squares) and ii) bound to DNA-3WJ/SWNT (red circles).

While YOYO-1 was not fluorescent when it is free in aqueous solution, DNA-3WJ/SWNT nanohybrid to which the same amount of YOYO-1 was added had a strong fluorescence intensity. Utilization of a DNA nanostructure not only allowed the self-assembly of SWNTs into a controlled branched nanostructure, it also acted as a functional group that enables the fluorescent labelling of SWNTs.

An alternative design approach to prepare DNA-3WJ/SWNT nanohybrids was also investigated where individual ssDNA strands designed to form the 3WJ were ultrasonicated with SWNTs first, followed by the annealing of ssDNA wrapped SWNTs (Figure 28). While we hypothesized that a similar DNA-3WJ/SWNT nanohybrid structure may form using this post-annealing preparation method, characterization of the prepared product predicted a different nanostructure.

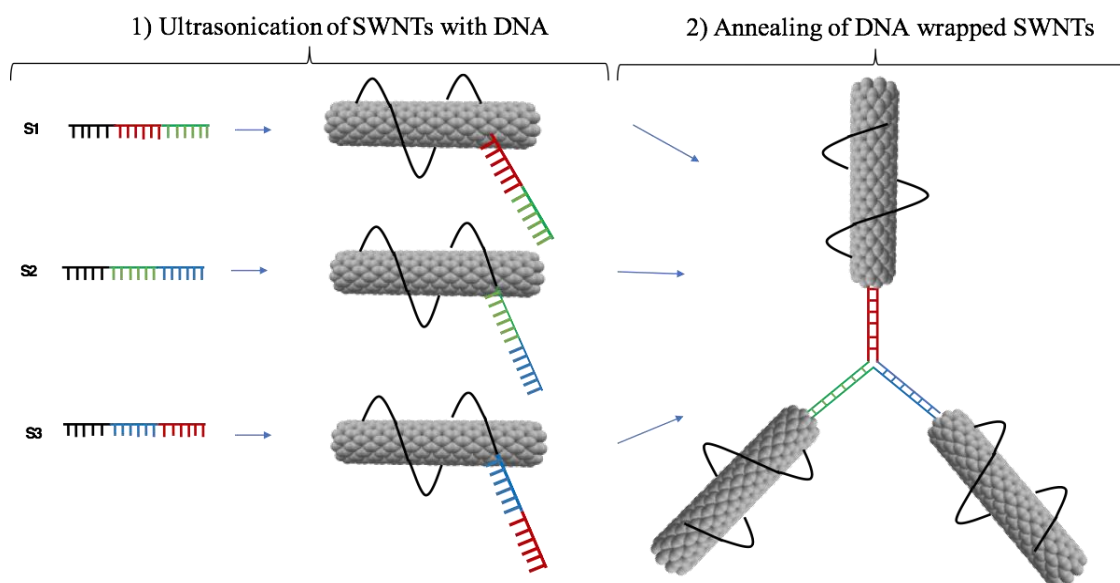


Figure 28. Schematic representation of the hypothesized mechanism of formation of DNA-3WJ/SWNT nanostructures with the post-annealing method.

Prepared DNA-3WJ/SWNT were characterized with agarose gel electrophoresis. While nanostructures formed by the pre-annealing method entered the gel and migrated, nanostructures formed by the post-annealing method were not able to enter the gel (Figure 29a). DNA-3WJ/SWNT nanostructures prepared with the post-annealing method remained in the loading well indicating a significantly larger molecular weight that limits the mobility of the nanostructure within the gel. Similarly, characterization of the average hydrodynamic diameter of the nanostructures formed by the post-annealing method predicted a bulky structure with a diameter that is several folds larger than the DNA-3WJ/SWNT nanohybrids formed by the pre-annealing method (Figure 29b). These results indicated that the post-annealing method resulted in a network of DNA-3WJ linked SWNTs instead of individual three-armed SWNT hybrids. Microscopic characterization of resulting nanostructures further confirmed the formation of such a network of SWNTs (Figure 30a and 30b). SWNTs, mostly self-assembled into junctions, appeared to be interconnected to each other forming a web-like structure composed of hexagons. When the two-dimensional planar 3WJ-SWNT nanostructures were linked at different angles, a three-dimensional network of SWNTs was possibly formed, as also visible on the microscopy images. A possible mechanism of formation of this SWNT network structure is demonstrated in Figure 30c. If multiple ssDNA strands wrap the same SWNT through the poly-G regions during the ultrasonication process, then SWNTs with multiple overhang sequences can form which will be linked into a network when the

complementary overhang sequences hybridize during the annealing step. When the pre-annealing method is applied, on the other hand, the rigid and bulky nature of the 3WJ implies a steric hindrance that prevents the wrapping of SWNTs by multiple 3WJ nanostructures which is not the case when SWNTs are ultrasonicated with linear ssDNA strands. Thus, we have demonstrated that the order of addition of the ssDNA strands that form the DNA-3WJ nanostructure and SWNTs can determine the structure of the DNA-3WJ/SWNT nanostructures. SWNTs self-assembled into Y-junctions or into a network composed of Y-junctions can be obtained in a controllable fashion by applying different methods.

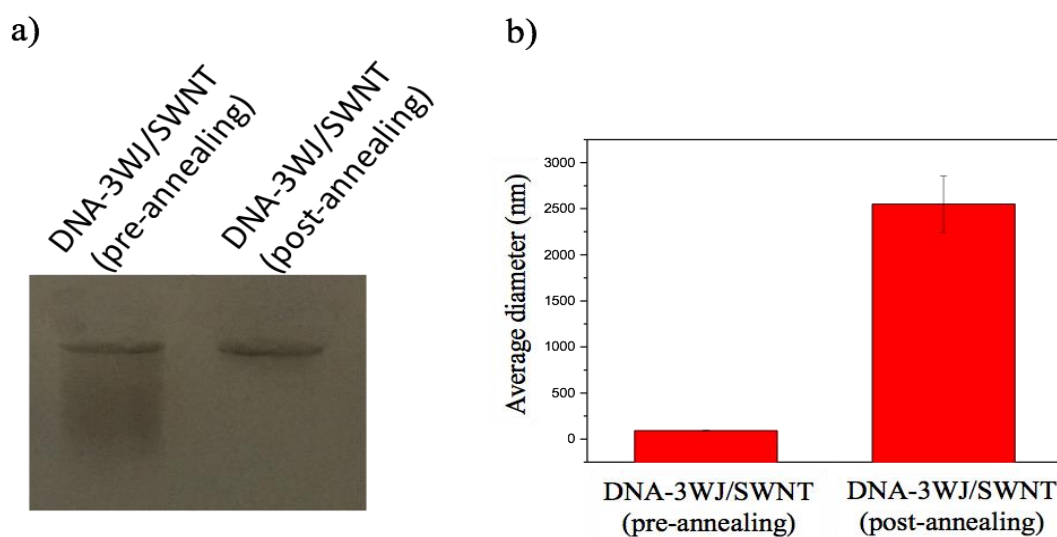


Figure 29. a) Visualization of an agarose gel loaded with DNA-3WJ/SWNT hybrid nanostructure prepared with pre-annealing (left) and post-annealing (right) methods. b) Average hydrodynamic diameters of DNA-3WJ/SWNT nanostructure prepared with pre-annealing (left) and post-annealing (right) methods.

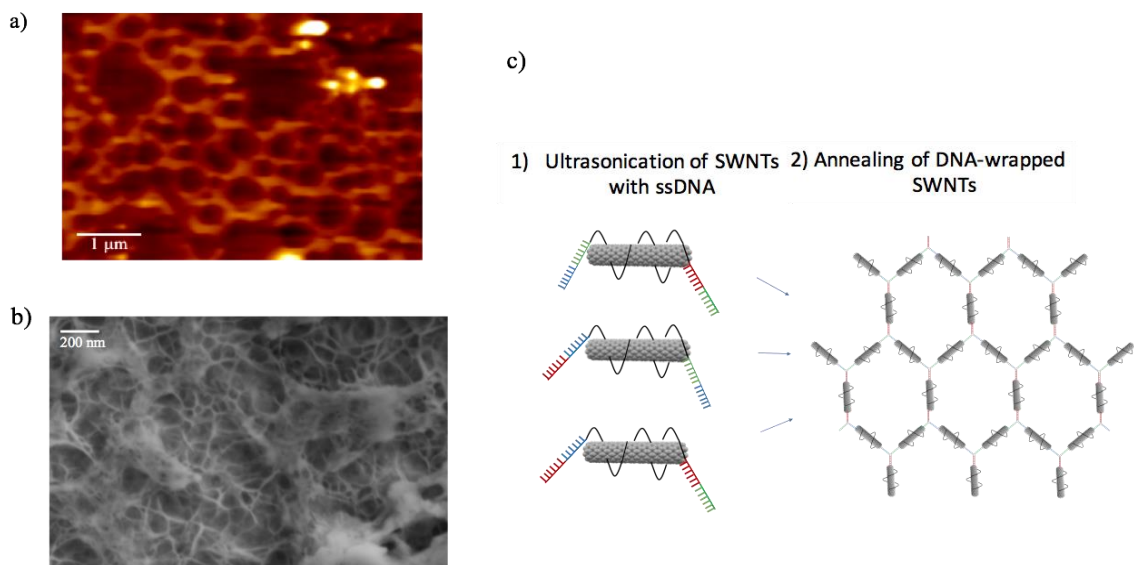


Figure 30. a) A representative AFM image of DNA-3WJ/SWNT nanostructures prepared with the post-annealing method. b) A representative SEM image of DNA-3WJ/SWNT nanostructures prepared with the post-annealing method. c) A schematic representation of the potential mechanism of formation of the network structure when the post-annealing method is used.

Photothermal properties of DNA-3WJ/SWNT nano hybrids were studied by measuring their NIR laser activated temperature elevations. Figure 31a demonstrated the rise in temperature generated by irradiation of SWNTs and DNA-3WJ/SWNT nano hybrids with 808 nm laser light for 15 minutes which indicate their photothermal properties as light-activated photothermal agents. DNA-3WJ/SWNT nano hybrids showed an extra 9°C temperature elevation and reached approximately 89°C while dispersion of SWNTs achieved only 80°C under identical conditions. Thus, the arrangement of SWNTs into dendrimer nanostructures increased their heat generation capacity relative to individual SWNTs. These results prove the main reason for enhanced temperature elevation which arose from branched SWNTs nanostructures as a consequence of photothermal effect of hybrids. DNA-3WJ/SWNT nano hybrids which were previously exposed to NIR laser light was irradiated again for the second time to investigate their stability at elevated temperature. However, the hybrids did not achieve the temperature which they reached in the first cycle due to the dissociation of dendrimer nanostructures (Figure 31b).

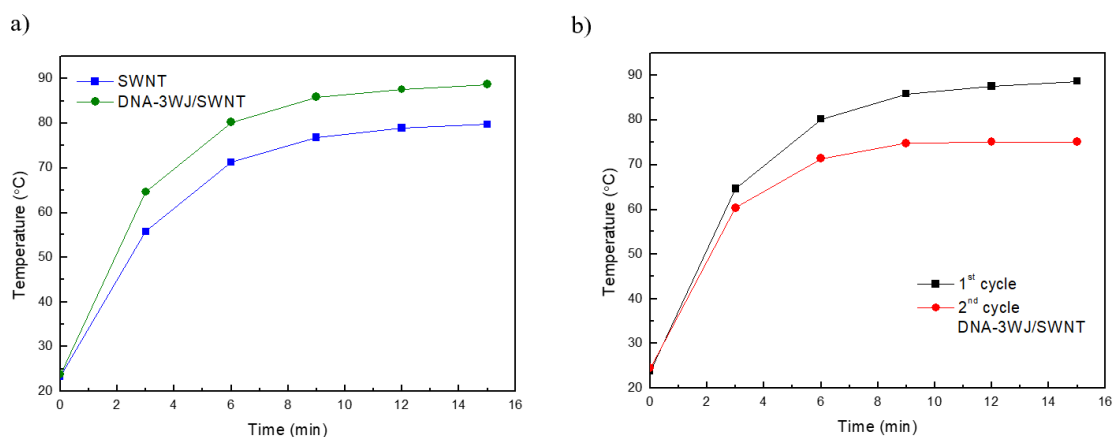


Figure 31. a) Time-temperature curves of SWNT and DNA-3WJ/SWNT containing equal SWNT concentration generated by 808 nm NIR laser irradiation for 15 min. b) Time-temperature curves generated by 808 nm NIR laser irradiation of the same DNA-3WJ/SWNT nanohybrid sample for two consequent cycles.

CHAPTER 4. FLUOROPHORE-DECORATED CARBON NANOTUBES AS SUNLIGHT ACTIVATING PHOTOTHERMAL AGENTS

4.1. Introduction

Energy demand is a continuously growing problem across the world which is expected to increase by approximately 1.5-3 times until 2050 [131-134]. Harvesting solar energy is one the most appealing strategies for green energy technologies because many scientists believe that the sun is the only promising candidate by offering a sustainable and affordable solution for the energy crisis, especially in the developing countries. Nanotechnology has attracted a great deal of attention in the development of active nanoparticles for solar thermal energy applications. Sunlight activated nanoparticles with high heat generation capacity has recently been emerging aspect of solar thermal collectors. These particles have been employed as nanofluids for steam generation system, tumor inhibition and catalysis [135-137]. Various advanced solar photothermal nanoparticles with broad light absorption have been developed in recent years such as plasmonic nanoparticles, CNTs, graphene oxide and polymers [138-140]. In this regard, several comprehensive studies have been established on the remarkable advantages of carbon-based materials over expensive plasmonic metal nanoparticles in terms of the photothermal conversion efficiency under sunlight illumination [141]. Moreover, carbon-based materials with much better stability under sunlight compared to polymers are promising nanoparticles for steam generation systems due to their low cost, low toxicity and easy availability.

Neuman et. al. developed steam-based solar autoclaves driven by light absorbing Au nanoparticles for inactivation of the pathogenic microorganism, distillation and desalination applications [142]. By this approach, the local temperature elevation induced direct steam generation without heating the liquid. They reported that when light-absorbing nanoparticles appropriately illuminated by sunlight, 80% of absorbed solar energy is transferred into water vapor which formed around the nanoparticles. Less than 20% of absorbed light energy is responsible for the heating of the liquid as a parallel effect. It means that these nanoparticles with strong photothermal response serve as boiling nucleation sites which can be used in water purification systems or destroying

bacteria and viruses [138, 143]. As pointed out by authors, this irreversible destruction of pathogenic species is originated from the formation of hot zone on the surface of nanoparticles under sunlight illumination.

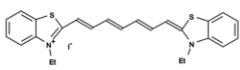
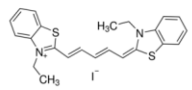
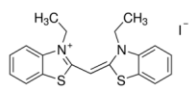
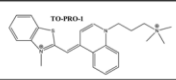
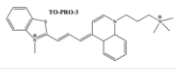
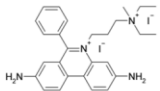
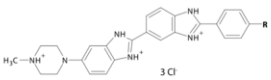
To the extent of our knowledge, there are no studies focusing on the enhancement of solar absorption capacity of CNTs to kill bacteria by creating broadband light-harvesting nanohybrids as solar photothermal agents. In this study, we extended our previous work and attempt to decorate CNTs with multiple fluorophores to achieve intense and broader absorption in UV, Vis and NIR regions. Here, we proposed specially designed sunlight activated CNT/Fluorophores nanohybrids to harvest a wide range of the solar spectrum for the photothermal destruction of bacteria.

4.2. Experimental

4.2.1. Materials

The materials mentioned in the experimental part of Chapter 2 were also used in this study. DWNTs with 2-4 nm outer diameter, 5-30 μm length and 60 wt. % purity were provided by Cheap Tubes Inc. (Cambridgeport, VT, USA). The fluorophores decorated on CNTs are listed in Table 2. TO-PRO-1 and TO-PRO-3 were purchased from Life Technologies (Carlsbad, CA, USA). 3,3'-diethylthiacyanine iodide (Disc₂(1), 97%) and Diethylthiadiazocyanine iodide (Disc₂(5), 98%) were purchased from Sigma Aldrich (Germany). Propidium iodide was purchased from MP Biomedicals (Solon, Ohio, USA). Hoechst was purchased from Thermo Scientific (Germany).

Table 2 The fluorophores that have been utilized to create sunlight activated CNT nano hybrids

Fluorophores	Chemical structure	Abs _{max} (nm)
Diethylthiadicarbocyanine iodide (DTTC)		770
Diethylthiadiazocyanine iodide (Disc ₂ 5)		646
3,3'-Diethylthiacyanine iodide (Disc ₂ 1)		424
TO-PRO-1		515
TO-PRO-3		642
Propidium iodide (PI)		535
Hoechst		~350

4.2.2. Preparation of CNT/Fluorophores Nano hybrids

An aqueous solution of Disc₂(1), Disc₂(5) and DTTC fluorophores with equal concentrations (50 μM) was prepared in DMSO which cover the UV, visible and NIR regions of the spectrum. 10 mL of a dispersal solution containing a mixture of fluorophores and 0.1 mg/mL DWNTs and MWNTs, respectively, was sonicated in ice

with microprobe (QSonica, Q700) for 20 min with 4 s pulse on and 5 s pulse off time at a power of 4-5 W. The centrifuge and filtration procedures were followed as previously described (Chapter 2). The similar sunlight absorbing nanohybrid was designed with the aqueous solution of 20 μM (TO-PRO-1)-(TO-PRO-3) and 50 μM Hoechst-PI fluorophores by following the same method. Concentration of CNT and CNT/Fluorophore dispersions were determined by absorbance spectroscopy (Cary 5000 Spectrophotometer) using the specific extinction coefficient for MWNTs at 500 nm ($\epsilon_{500} = 46 \text{ mL mg}^{-1} \text{ cm}^{-1}$).

4.2.3. Characterization of CNT/Fluorophores nanohybrids

Absorbance spectroscopy was performed to confirm the increase in absorbance capacity after nanohybrid formation. Samples were scanned in a quartz cuvette in the wavelength range of 200 to 1000 nm.

Florescence spectra of nanohybrids were obtained with a Cary Eclipse Fluorescence Spectrophotometer. Fluorophores and CNT/Fluorophores nanohybrids were scanned in a quartz cuvette at 420, 650 and 720 nm according to the excitation maximum of Disc₂(1), Disc₂(5) and DTTC, respectively.

4.2.3.1. Sunlight activated heating in CNT/Fluorophores nanohybrids

The dispersions of CNT and CNT/Fluorophores nanohybrids were diluted to the same CNT concentrations (0,019 mg/mL for MWNT and 0,007 mg/mL for DWNT) to compare their heat generation capacity more accurately. 2 mL of fluorophore mixture along with CNT and CNT/Fluorophores dispersions were exposed to artificial solar light obtained by the solar simulator (LCS-100TM M94011A-ES, Oriel Instruments). The distance between the sample and the light source has been fixed correspond to 1 sun output power. Temperature was recorded every three min with a thermocouple placed inside the dispersion as seen in Figure 32 (Hanna HI 935005 K-Thermocouple Thermometer).



Figure 32. Experimental setup for the measurement of photothermal conversion by solar simulator.

4.3. Results and Discussions

Sunlight harvesting nanostructures composed of CNTs decorated with multiple fluorophores are presented. These dyes possess tunable light absorption over a wide range of solar spectrum which allows for spectral compatibility in a wide range of applications. Li et al. pioneered the utilization of fluorophores as key components in luminescent solar concentrators to improve the sunlight harvesting performance by reducing self-reabsorption of emitted light [144]. Herein, we for the first time have improved sunlight harvesting efficiency of CNTs by decorating their surface with multiple fluorophores for the utilization of both solar thermal collectors and antibacterial materials. CNTs were sonicated with an aqueous solution of fluorophores. Resulting sonicated mixtures were ultracentrifuged and filtered to remove bundled CNTs and unbound dye molecules, respectively. Fluorophore molecules has conferred water solubility to CNTs interacting with their aromatic structure through π - π stacking and Van der Waals interaction. Thus, the decoration of CNTs with fluorophores resulted in sunlight activated photothermal agents.

The characterization of non-covalent interactions between fluorophores and CNTs was performed by absorption spectroscopy. The absorption spectrum of DWNT/Disc₂(1)-Disc₂(5)-DTTC and MWNT/Disc₂(1)-Disc₂(5)-DTTC in comparison to the spectrum of DWNT and MWNT demonstrated an enhanced absorbance with the formation of nanohybrids in the wavelength range of 250-1000 nm (Figure 33). Non-covalent binding

interaction acquired new absorption peaks to the nanohybrids in UV, Vis and NIR regions at which pristine CNTs do not normally absorb light. The maximum increment of absorption capacity was shown in MWNT/Disc₂(1)-Disc₂(5)-DTTC. This enhancement indicates the strong interaction between fluorophores and MWNTs accompanied by a better dispersion of MWNTs.

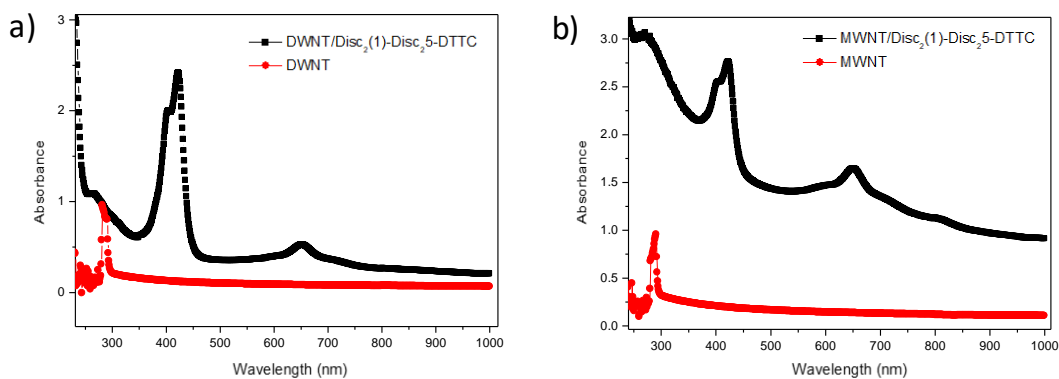


Figure 33. Absorbance spectra of DWNT/Disc₂(1)-Disc₂(5)-DTTC and MWNT/Disc₂(1)-Disc₂(5)-DTTC nanohybrids.

Figure 34 shows the change in electronic structure on CNTs with the nanohybrid formation. The normalized absorption spectra of fluorophores and CNT/Fluorophores nanohybrids exhibited significant differences due to non-covalent interaction between fluorophores and CNTs. As seen in each spectrum, these interactions introduced a slight increase in absorption toward lower wavelengths which corresponds to the dimeric forms of fluorophores. It proves the arrangement of fluorophores on CNTs scaffold resulting in sunlight absorbing nanohybrids. However, the absorption peak of DTTC on CNT/Fluorophore nanohybrids has not been observed. Possible reasons for this are still being investigated.

The formation of sunlight activated photothermal nanohybrids was also examined with an other fluorophore set, (TO-PRO-1)-(TO-PRO-3)-Hoechst-PI. However, the binding affinity between this fluorophore mixture and DWNT was inadequate to obtain high dispersion quality. This was confirmed by the lower absorption capacity of DWNT/(TO-PRO-1)-(TO-PRO-3)-Hoechst-PI nanohybrids compared to DWNTs dispersed in a surfactant solution (Figure 35a).

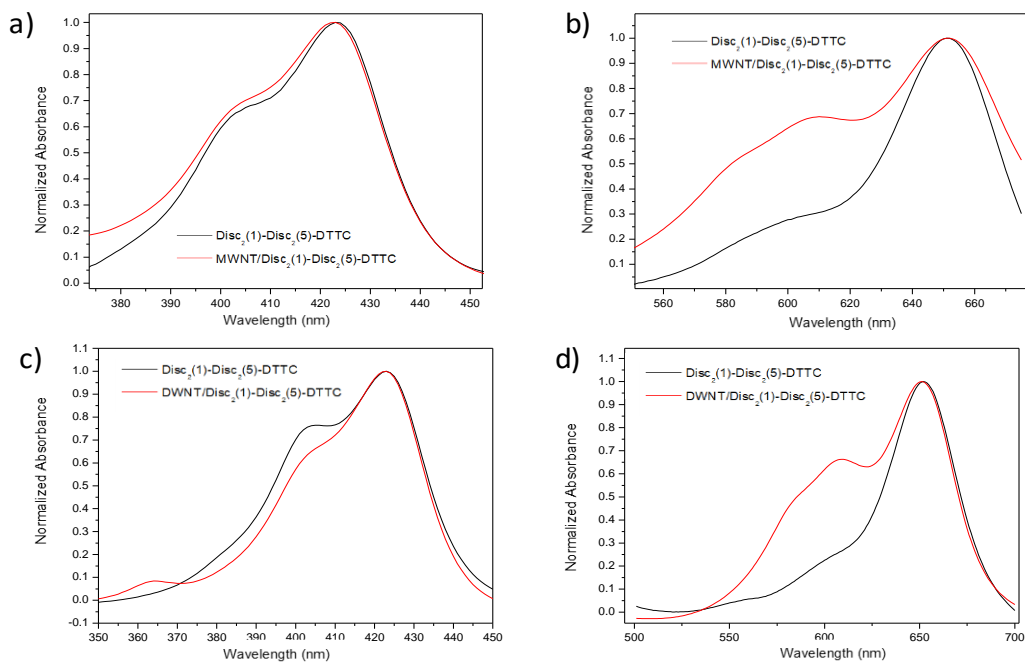


Figure 34. a) Normalized absorbance spectra of Disc₂(1)-Disc₂(5)-DTTC and MWNT/Disc₂(1)-Disc₂(5)-DTTC in the range of Disc₂(1) absorption containing equal concentration of fluorophore solution. b) Normalized absorbance spectra of Disc₂(1)-Disc₂(5)-DTTC and MWNT/Disc₂(1)-Disc₂(5)-DTTC in the range of Disc₂(5) absorption containing equal concentration of fluorophore solution. c) Normalized absorbance spectra of Disc₂(1)-Disc₂(5)-DTTC and DWNT/Disc₂(1)-Disc₂(5)-DTTC in the range of Disc₂(1) absorption containing equal concentration of fluorophore solution. d) Normalized absorbance spectra of Disc₂(1)-Disc₂(5)-DTTC and DWNT/Disc₂(1)-Disc₂(5)-DTTC in the range of Disc₂(5) absorption containing equal concentrations of fluorophore solution.

Some interesting results have emerged from the comparison between the absorption spectra of free fluorophores and their hybrids with CNTs (Figures 35b, 35c and 35d). Only Hoechst provoked a change in electronic structure of sidewalls of DWNT through the hybrid formation; on the other hand, we did not encounter such change on other fluorophores. It demonstrated that the non-covalent interaction between fluorophores and CNTs only arose between Hoechst and DWNTs while other fluorophores did not interact with DWNTs. For this reason, sunlight absorbing nanohybrids in the wide spectrum range were not obtained with the fluorophores of (TO-PRO-1), (TO-PRO-3), Hoechst and PI.

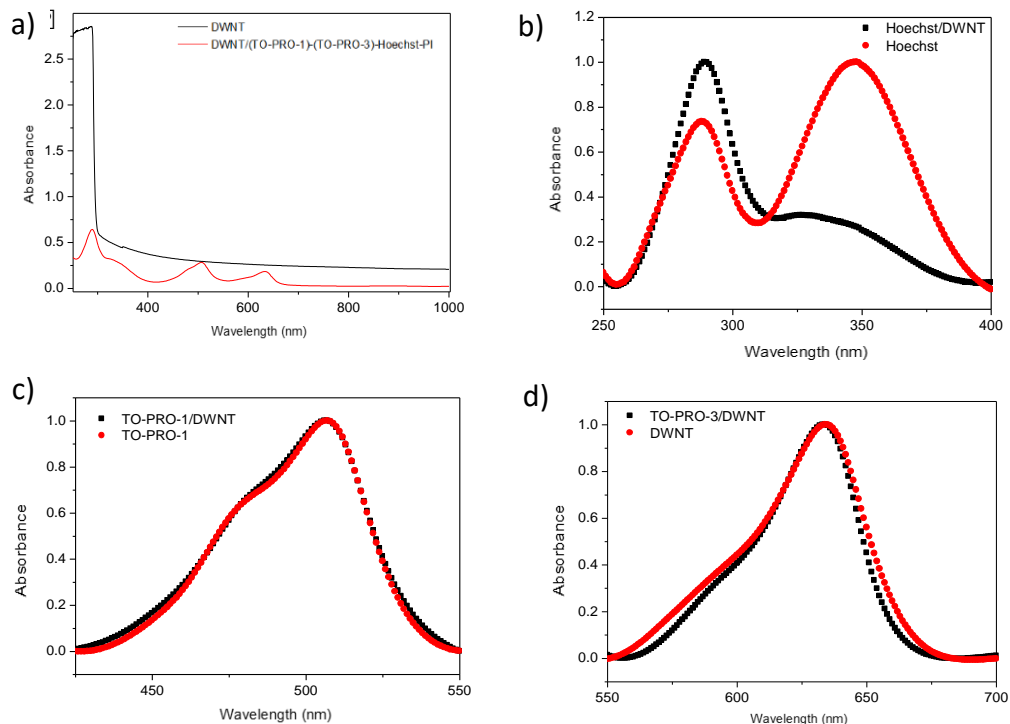


Figure 35. Absorbance spectra of DWNT and DWNT/(TO-PRO-1)-(TO-PRO-3)-Hoechst-PI nanohybrids containing equal concentration of DWNTs. (a), and absorbance spectra of (TO-PRO-1)-(TO-PRO-3)-Hoechst-PI and DWNT/(TO-PRO-1)-(TO-PRO-3)-Hoechst-PI containing equal concentration of fluorophore solution in the range of corresponding fluorophore absorption.

Figure 36 demonstrates the fluorescence spectrum of MWNT/Disc₂(1)-Disc₂(5)-DTTC with respect to the spectrum of Disc₂(1)-Disc₂(5)-DTTC in order to analyze the light-heat conversion of nanohybrids. As we hypothesized, the fluorescence emission of free Disc₂(1)-Disc₂(5)-DTTC was quenched upon binding to MWNTs, leading to efficient photothermal conversion with high heat generation capacity. The conversion of all absorbed sunlight into heat energy is a consequence of electron-energy transfer indicating the promising photothermal properties of MWNT/Disc₂(1)-Disc₂(5)-DTTC nanohybrids.

The photothermal properties of prepared nanohybrids was examined by measuring temperature elevation under one sun light illumination for 15 minutes (Figure 37a and 37b). Dispersion of MWNTs and MWNT/Disc₂(1)-Disc₂(5)-DTTC nanohybrids exposed to artificial sunlight provided by solar simulator which triggered the light to heat conversion. Both DWNT/Disc₂(1)-Disc₂(5)-DTTC and MWNT/Disc₂(1)-Disc₂(5)-DTTC nanohybrids showed enhanced temperature elevation relative to dispersions of DWNTs and MWNTs after 15 minutes of irradiation. While there were no significant temperature

differences between the dispersion of MWNTs and free fluorophores, the array of fluorophore molecules on MWNTs enabled to reach 50°C. These results prove the actual cause of temperature elevation that originated from sunlight absorbing nanoarrays on CNTs, enabling the utilization of these photothermal agents as antimicrobial nanomaterials.

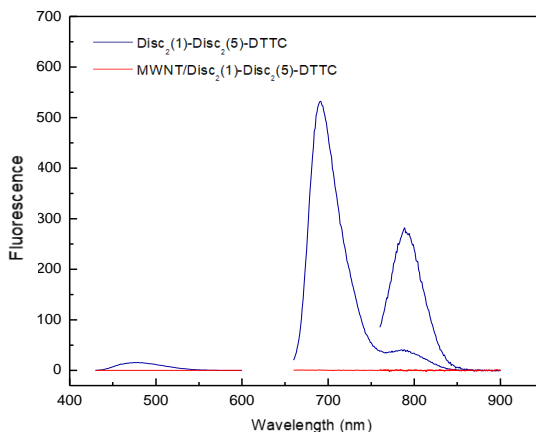


Figure 36. Fluorescence spectra of $\text{Disc}_2(1)\text{-Disc}_2(5)\text{-DTTC}$ and $\text{MWNT/Disc}_2(1)\text{-Disc}_2(5)\text{-DTTC}$ containing equal concentration of fluorophore solution.

Time-temperature curve of $\text{DWNT}/(\text{TO-PRO-1})\text{-}(\text{TO-PRO-3})\text{-Hoechst-PI}$ nanohybrids was also obtained under the same condition to determine the photothermal properties of alternative nanohybrid structure (Figure 37c). Even though $\text{DWNT}/(\text{TO-PRO-1})\text{-}(\text{TO-PRO-3})\text{-Hoechst-PI}$ nanohybrids showed a remarkable temperature elevation relative to the dispersion of fluorophores, the temperature elevation of the prepared nanohybrids was only 10°C higher than that of the dispersion of DWNTs. It indicates that this nanohybrid did not have a broad absorption capacity in the wide spectrum range which is consistent with previous result. Further improvements should be investigated for the utilization of $\text{DWNT}/(\text{TO-PRO-1})\text{-}(\text{TO-PRO-3})\text{-Hoechst-PI}$ nanohybrids as sunlight harvesting photothermal agents. In this context, the intrinsic properties of carbon nanotubes such as purity, length and chirality, the concentration of carbon nanotubes and fluorophores and/or the sonication time and power should be optimized to enhance the absorption of CNTs and the self-assembly capacity of fluorophores on CNTs [145]. However, more work is needed for this ongoing project, thus we focused on $\text{Disc}_2(1)$, $\text{Disc}_2(5)$ and DTTC fluorophores and their hybrids with CNTs for further analysis.

The potential of $\text{DWNT/Disc}_2(1)\text{-Disc}_2(5)\text{-DTTC}$ and $\text{MWNT/Disc}_2(1)\text{-Disc}_2(5)\text{-DTTC}$ nanohybrids as multiple-use photothermal agents was also investigated by exposing the

same nanohybrids to the sunlight for the second time under the same condition (Figure 38). The time-temperature curves of both nanohybrids at the end of the second irradiation cycle were matched with their first curve. It demonstrated that both nanohybrids keep their integrity even at elevated temperature and remain stable after two rounds of sunlight irradiation. These results show that DWNT/Disc₂(1)-Disc₂(5)-DTTC and MWNT/Disc₂(1)-Disc₂(5)-DTTC nanohybrids have high potential to reach the elevated temperature as multiuse photothermal agents for two cycles.

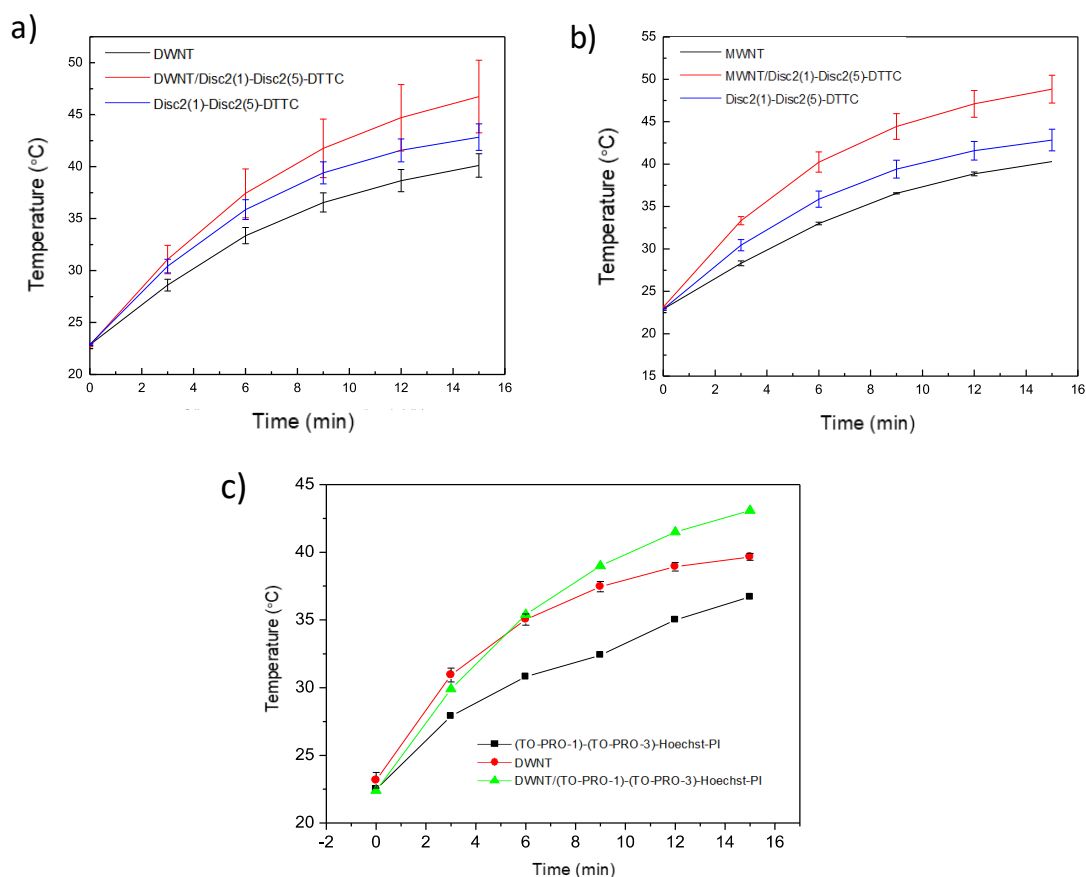


Figure 37. Time-temperature curves of (a) DWNT, DWNT/ Disc₂(1)-Disc₂(5)-DTTC and Disc₂(1)-Disc₂(5)-DTTC, (b) MWNT, MWNT/ Disc₂(1)-Disc₂(5)-DTTC and Disc₂(1)-Disc₂(5)-DTTC, (c) DWNT, DWNT/(TO-PRO-1)-(TO-PRO-3)-Hoechst-PI and (TO-PRO-1)-(TO-PRO-3)-Hoechst-PI containing equal fluorophores and CNT concentration generated under 1 sun illumination for 15 min.

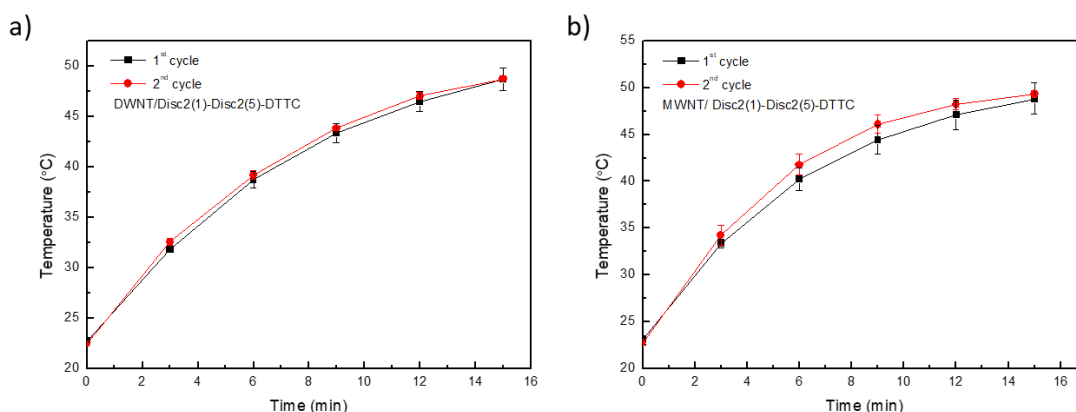


Figure 38. Time-temperature curves obtained under one sun illumination of the same DWNT/ Disc₂(1)-Disc₂(5)-DTTC and MWNT/ Disc₂(1)-Disc₂(5)-DTTC nanohybrid samples for two consequent cycles.

All these results indicated that these nanohybrids possess high heat generation capacity by irradiation of simulated sunlight. According to our preliminary results, these nanomaterials are promising candidate as sunlight activated photothermal agents for killing the pathogenic bacteria. However, the antibacterial activity of nanohybrids is ongoing research which requires more work and further improvements. Non-covalent interaction between the fluorophores and CNTs should be optimized to improve the temperature elevation that is accompanied by increased killing efficiency.

CHAPTER 5. CONCLUSIONS

Two novel methods to improve light absorption capacity of CNTs for utilization of these nanoparticles as photothermal agents in the effective killing of bacteria were introduced. These methods describe the decoration of CNTs surface with arrays of fluorophores and the self-assembly of three individual SWNTs into a DNA 3WJ which increase the amount of light absorbed by prepared CNT/Fluorophore and DNA-3WJ/SWNT nanohybrids. While NIR light absorbing fluorophores were self-assembled on CNTs through strong noncovalent interactions in the first method, the other technique describes the arrangement of three individual SWNTs into dendrimeric nanostructures with the guidance of DNA self-assembly. We designed sunlight harvesting nanohybrids through the self-assembly of visible light absorbing fluorophores on the CNTs surface to activate these nanoparticles with sunlight as well. Both approaches enhanced the photothermal properties of CNTs resulting in higher heat generation efficiency than what occurred for pristine CNTs under identical conditions.

As the first method, NIR light absorbing fluorophores (DTTC) formed strong noncovalent interactions with MWNTs and formed a self-assembled array which acted as a light harvesting antenna increasing the amount of laser light absorbed by MWNT/DTTC nanohybrids. The enhanced light absorption by MWNT/DTTC nanohybrids was reflected as enhanced heat release resulting in elevated temperatures that can not be reached by MWNTs alone under the same laser irradiation conditions. Irradiation of *P.aeruginosa* suspensions in the presence of MWNT/DTTC nanohybrids results in 77% killing of bacteria through heat generated physical damage as demonstrated by SEM. Nanocomposites of waterborne PU and MWNT/DTTC were shown as potential antimicrobial and antibiofilm coating materials which can generate temperatures reaching 120°C and kill surface attached bacteria upon laser irradiation. As alternative photothermal agents, sunlight-activated CNT/Fluorophore nanohybrids were also demonstrated to present strong photothermal activity through their enhanced broadband absorption capacity.

Similarly, we presented the hybridization of SWNTs with DNA 3WJ nanostructures to improve their light absorption and heat generation capacity. Three individual SWNT molecules are linked into a junction at a controllable angle by the utilization of a two-

dimensional self-assembled DNA 3WJ nanostructure. While the DNA-3WJ was demonstrated to be a relatively better dispersing agent than a linear ssDNA analog, it also acted as an effective template for the arrangement of SWNTs into a desired nanostructure. The design of the DNA-3WJ/SWNT hybrids also allows the effective labeling of SWNTs with fluorophores. With a slight modification of the preparation method where the order of addition of components is changed, these SWNT junctions were interconnected, resulting in a web-like network of SWNTs. Hybrids of DNA-3WJ and SWNTs were shown as potential sunlight-activated photothermal agents which can generate temperature reaching 90°C within 15 minutes. Methods reported here provide an effective approach for the self-assembly of SWNTs in solution, utilizing self-assembled DNA nanostructures and can be applied to various other DNA nanostructures resulting in SWNT assemblies of different structures and dimensions. CNT based hybrid nanostructures and their surface coatings presented here have strong potential as antimicrobial and antibiofilm nanomaterials effective on antibiotic-resistant bacteria.

REFERENCES

1. Wright, G.D., *Molecular mechanisms of antibiotic resistance*. Chem Commun (Camb), 2011. **47**(14): p. 4055-61.
2. Gao, J., H. Gu, and B. Xu, *Multifunctional Magnetic Nanoparticles: Design, Synthesis, and Biomedical Applications*. Accounts of Chemical Research, 2009. **42**(8): p. 1097-1107.
3. Doane, T.L. and C. Burda, *The unique role of nanoparticles in nanomedicine: imaging, drug delivery and therapy*. Chem Soc Rev, 2012. **41**(7): p. 2885-911.
4. Singh, R. and S.V. Torti, *Carbon nanotubes in hyperthermia therapy*. Adv Drug Deliv Rev, 2013. **65**(15): p. 2045-60.
5. Russell, A.D., *Lethal effects of heat on bacterial physiology and structure*. Science Progress (1933-), 2003. **86**(1/2): p. 115-137.
6. Jaque, D., et al., *Nanoparticles for photothermal therapies*. Nanoscale, 2014. **6**(16): p. 9494-530.
7. Tong, L., et al., *Gold Nanorods Mediate Tumor Cell Death by Compromising Membrane Integrity*. Adv Mater, 2007. **19**: p. 3136-3141.
8. Huang, X., et al., *Cancer Cell Imaging and Photothermal Therapy in the Near-Infrared Region by Using Gold Nanorods*. Journal of the American Chemical Society, 2006. **128**(6): p. 2115-2120.
9. Zhou, W., X. Liu, and J. Ji, *More efficient NIR photothermal therapeutic effect from intracellular heating modality than extracellular heating modality: an in vitro study*. Journal of Nanoparticle Research, 2012. **14**(9).
10. Zharov, V.P., et al., *Photothermal nanotherapeutics and nanodiagnostics for selective killing of bacteria targeted with gold nanoparticles*. Biophys J, 2006. **90**(2): p. 619-27.
11. He, J., et al., *Self-assembly of amphiphilic plasmonic micelle-like nanoparticles in selective solvents*. J Am Chem Soc, 2013. **135**(21): p. 7974-84.
12. Chou, C.-H., C.-D. Chen, and C.R.C. Wang, *Highly Efficient, Wavelength-Tunable, Gold Nanoparticle Based Optothermal Nanoconvertors*. The Journal of Physical Chemistry B, 2005. **109**(22): p. 11135-11138.
13. Link, S., et al., *Femtosecond transient-absorption dynamics of colloidal gold nanorods: Shape independence of the electron-phonon relaxation time*. Physical Review B, 2000. **61**(9): p. 6086-6090.

14. Kotaidis, V. and A. Plech, *Cavitation dynamics on the nanoscale*. Applied Physics Letters, 2005. **87**(21).
15. Wu, M.-C., et al., *Graphene-Based Photothermal Agent for Rapid and Effective Killing of Bacteria*. ACS Nano, 2013. **7**(2): p. 1281-1290.
16. Yang, K., et al., *Graphene in Mice: Ultrahigh In Vivo Tumor Uptake and Efficient Photothermal Therapy*. Nano Letters, 2010. **10**(9): p. 3318-3323.
17. Robinson, J.T., et al., *Ultrasmall Reduced Graphene Oxide with High Near-Infrared Absorbance for Photothermal Therapy*. Journal of the American Chemical Society, 2011. **133**(17): p. 6825-6831.
18. Kim, J.W., et al., *Photothermal antimicrobial nanotherapy and nanodiagnostics with self-assembling carbon nanotube clusters*. Lasers Surg Med, 2007. **39**(7): p. 622-34.
19. Akasaka, T., et al., *The bactericidal effect of carbon nanotube/agar composites irradiated with near-infrared light on Streptococcus mutans*. Materials Science and Engineering: B, 2010. **173**(1-3): p. 187-190.
20. Levi-Polyachenko, N., et al., *Eradicating group A streptococcus bacteria and biofilms using functionalised multi-wall carbon nanotubes*. Int J Hyperthermia, 2014. **30**(7): p. 490-501.
21. Ondera, T.J. and A.T. Hamme, 2nd, *Gold Nanopopcorn Attached Single-Walled Carbon Nanotube Hybrid for Rapid Detection and Killing of Bacteria*. J Mater Chem B, 2014. **2**(43): p. 7534-7543.
22. Liu, Z. and Z. Chen, *CHAPTER 9. Near Infrared Nanomaterials for Photothermal Therapy*, in *Near-infrared Nanomaterials*. 2016. p. 277-321.
23. Siregar, S., et al., *Application of single walled carbon nanotubes for heating agent in photothermal therapy*. 2016.
24. Kim, J.-W., et al., *Golden carbon nanotubes as multimodal photoacoustic and photothermal high-contrast molecular agents*. Nature Nanotechnology, 2009. **4**: p. 688.
25. Prencipe, G., et al., *PEG Branched Polymer for Functionalization of Nanomaterials with Ultralong Blood Circulation*. Journal of the American Chemical Society, 2009. **131**(13): p. 4783-4787.
26. Chakravarty, P., et al., *Thermal ablation of tumor cells with antibody-functionalized single-walled carbon nanotubes*. Proceedings of the National

- Academy of Sciences of the United States of America, 2008. **105**(25): p. 8697-8702.
27. Kam, N.W.S., et al., *Carbon nanotubes as multifunctional biological transporters and near-infrared agents for selective cancer cell destruction*. Proceedings of the National Academy of Sciences of the United States of America, 2005. **102**(33): p. 11600-11605.
 28. Ghosh, S., et al., *Increased Heating Efficiency and Selective Thermal Ablation of Malignant Tissue with DNA-Encased Multiwalled Carbon Nanotubes*. ACS Nano, 2009. **3**(9): p. 2667-2673.
 29. Maestro, L.M., et al., *Heating efficiency of multi-walled carbon nanotubes in the first and second biological windows*. Nanoscale, 2013. **5**(17): p. 7882-9.
 30. Robinson, J.T., et al., *High Performance In Vivo Near-IR (>1 μm) Imaging and Photothermal Cancer Therapy with Carbon Nanotubes*. Nano Res, 2010. **3**(11): p. 779-793.
 31. Williams, C.G., XXVI.—*Researches on Chinoline and its Homologues*. Transactions of the Royal Society of Edinburgh, 1857. **21**(3): p. 377-401.
 32. Patonay, G. and M.D. Antoine, *Near-Infrared Fluorogenic Labels: New Approach to an Old Problem*. Analytical Chemistry, 1991. **63**(6): p. 321A-327A.
 33. Deligeorgiev, T., *Molecular Probes Based on Cyanine Dyes for Nucleic Acid Research*. 1998. 125-139.
 34. Daehne, S., U. Resch-Genger, and O. Wolfbeis, *Near-Infrared Dyes for High Technology Applications*. Vol. 52. 1998.
 35. Armitage, B.A., *Cyanine Dye–DNA Interactions: Intercalation, Groove Binding, and Aggregation*, in *DNA Binders and Related Subjects*. 2005. p. 55-76.
 36. Marin, V.L., *Thermodynamic and Kinetic Investigation of Nucleic Acid Molecular Recognition by Synthetic Oligomers and Small Molecules*, in *Department of Chemistry*. 2005, Carnegie Mellon University.
 37. Blackburn, G.M., et al., *Nucleic Acids in Chemistry and Biology, 3rd Edition*. 2006: Royal Society of Chemistry. 470 pp.
 38. Gates, K.S., *Bioorganic Chemistry: Nucleic Acids Edited by Sidney M. Hecht (University of Virginia)*. Oxford University Press: New York. 1996. viii + 500 pp. \$59.95. ISBN 0-19-508467-5. Journal of the American Chemical Society, 1997. **119**(7): p. 1808-1808.

39. Geierstanger, B.H. and D.E. Wemmer, *Complexes of the Minor Groove of DNA*. Annual Review of Biophysics and Biomolecular Structure, 1995. **24**(1): p. 463-493.
40. Benveniste, A.L., *DNA Templated Supramolecular Assemblies of Cyanine Dyes*, in *Chemistry*. 2008, Carnegie Mellon University.
41. Sovenyhazi, K.M., *Spectroscopic studies of the multiple binding modes of a trimethine-bridged cyanine dye with DNA*. Nucleic Acids Research, 2003. **31**(10): p. 2561-2569.
42. Lee Linda, G., C.H. Chen, and A. Chiu Laura, *Thiazole orange: A new dye for reticulocyte analysis*. Cytometry, 1986. **7**(6): p. 508-517.
43. Netzel, T.L., et al., *Base-Content Dependence of Emission Enhancements, Quantum Yields, and Lifetimes for Cyanine Dyes Bound to Double-Strand DNA: Photophysical Properties of Monomeric and Bichromophoric DNA Stains*. The Journal of Physical Chemistry, 1995. **99**(51): p. 17936-17947.
44. Silva, G.L., et al., *Experimental and Computational Investigation of Unsymmetrical Cyanine Dyes: Understanding Torsionally Responsive Fluorogenic Dyes*. Journal of the American Chemical Society, 2007. **129**(17): p. 5710-5718.
45. Hannah, K.C. and B.A. Armitage, *DNA-Templated Assembly of Helical Cyanine Dye Aggregates: A Supramolecular Chain Polymerization*. Accounts of Chemical Research, 2004. **37**(11): p. 845-853.
46. Garoff, R.A., et al., *Helical Aggregation of Cyanine Dyes on DNA Templates: Effect of Dye Structure on Formation of Homo- and Heteroaggregates*. Langmuir, 2002. **18**(16): p. 6330-6337.
47. Seifert, J.L., et al., *Spontaneous Assembly of Helical Cyanine Dye Aggregates on DNA Nanotemplates*. Journal of the American Chemical Society, 1999. **121**(13): p. 2987-2995.
48. Kuhn, H. and C. Kuhn, *CHROMOPHORE COUPLING EFFECTS*, in *J-Aggregates*. 1996, WORLD SCIENTIFIC. p. 1-40.
49. Karlsson, H.J., P. Lincoln, and G. Westman, *Synthesis and DNA binding studies of a new asymmetric cyanine dye binding in the minor groove of [poly(dA-dT)]₂*. Bioorganic & Medicinal Chemistry, 2003. **11**(6): p. 1035-1040.

50. McRae, E.G. and M. Kasha, *Enhancement of Phosphorescence Ability upon Aggregation of Dye Molecules*. The Journal of Chemical Physics, 1958. **28**(4): p. 721-722.
51. Kasha, M., H. Rawls, and M. Ashraf El-Bayoumi, *The exciton model in molecular spectroscopy*, *Pure Appl. Chem.* **11**, 371-392. Vol. 11. 1965. 371-392.
52. Davydov, A.S., *THE THEORY OF MOLECULAR EXCITONS*. Soviet Physics Uspekhi, 1964. **7**(2): p. 145.
53. West, W. and S. Pearce, *The Dimeric State of Cyanine Dyes*. The Journal of Physical Chemistry, 1965. **69**(6): p. 1894-1903.
54. Cavuslar, O. and H. Unal, *Self-assembly of DNA wrapped carbon nanotubes and asymmetrical cyanine dyes into fluorescent nanohybrids*. RSC Advances, 2015. **5**(29): p. 22380-22389.
55. Dai, H., *Carbon Nanotubes: Synthesis, Integration, and Properties*. Accounts of Chemical Research, 2002. **35**(12): p. 1035-1044.
56. Ouyang, M., J.-L. Huang, and C.M. Lieber, *Fundamental Electronic Properties and Applications of Single-Walled Carbon Nanotubes*. Accounts of Chemical Research, 2002. **35**(12): p. 1018-1025.
57. Barone, P.W. and M.S. Strano, *Reversible control of carbon nanotube aggregation for a glucose affinity sensor*. Angew Chem Int Ed Engl, 2006. **45**(48): p. 8138-41.
58. Balasubramanian, K. and M. Burghard, *Chemically functionalized carbon nanotubes*. Small, 2005. **1**(2): p. 180-92.
59. Banerjee, S., T. Hemraj-Benny, and S.S. Wong, *Covalent Surface Chemistry of Single-Walled Carbon Nanotubes*. Advanced Materials, 2005. **17**(1): p. 17-29.
60. Banerjee, S., M.G. Kahn, and S.S. Wong, *Rational chemical strategies for carbon nanotube functionalization*. Chemistry, 2003. **9**(9): p. 1898-908.
61. Zorbas, V., et al., *Importance of Aromatic Content for Peptide/Single-Walled Carbon Nanotube Interactions*. Journal of the American Chemical Society, 2005. **127**(35): p. 12323-12328.
62. Fan, C., *DNA Nanotechnology: From Structure to Function*. 2013: Springer Berlin Heidelberg.
63. Coleman, J.N., U. Khan, and Y.K. Gun'ko, *Mechanical Reinforcement of Polymers Using Carbon Nanotubes*. Advanced Materials, 2006. **18**(6): p. 689-706.

64. Zheng, M., et al., *DNA-assisted dispersion and separation of carbon nanotubes*. Nat Mater, 2003. **2**(5): p. 338-42.
65. Zheng, M., et al., *Structure-Based Carbon Nanotube Sorting by Sequence-Dependent DNA Assembly*. Science, 2003. **302**(5650): p. 1545.
66. Rothemund, P.W., *Folding DNA to create nanoscale shapes and patterns*. Nature, 2006. **440**(7082): p. 297-302.
67. Douglas, S.M., et al., *Self-assembly of DNA into nanoscale three-dimensional shapes*. Nature, 2009. **459**(7245): p. 414-8.
68. Ding, B., et al., *Gold Nanoparticle Self-Similar Chain Structure Organized by DNA Origami*. Journal of the American Chemical Society, 2010. **132**(10): p. 3248-3249.
69. McMorrow, J., M. Freeley, and M. Palma, *DNA-Wrapped Single-Walled Carbon Nanotube Assemblies*. Industrial & Engineering Chemistry Research, 2017. **56**(18): p. 5302-5308.
70. Han, S.P., et al., *DNA-linker-induced surface assembly of ultra dense parallel single walled carbon nanotube arrays*. Nano Lett, 2012. **12**(3): p. 1129-35.
71. Um, S.H., et al., *Enzyme-catalysed assembly of DNA hydrogel*. Nat Mater, 2006. **5**(10): p. 797-801.
72. Xing, Y., et al., *Self-assembled DNA hydrogels with designable thermal and enzymatic responsiveness*. Adv Mater, 2011. **23**(9): p. 1117-21.
73. Cheng, E., et al., *A pH-triggered, fast-responding DNA hydrogel*. Angew Chem Int Ed Engl, 2009. **48**(41): p. 7660-3.
74. You, M., et al., *Engineering DNA aptamers for novel analytical and biomedical applications*. Chemical Science, 2011. **2**(6).
75. Liedl, T., et al., *Controlled trapping and release of quantum dots in a DNA-switchable hydrogel*. Small, 2007. **3**(10): p. 1688-93.
76. Cheng, E., et al., *DNA-SWNT hybrid hydrogel*. Chem Commun (Camb), 2011. **47**(19): p. 5545-7.
77. Norrby, S.R., C.E. Nord, and R. Finch, *Lack of development of new antimicrobial drugs: a potential serious threat to public health*. The Lancet Infectious Diseases, 2005. **5**(2): p. 115-119.
78. Leeb, M., *A shot in the arm*. Nature, 2004. **431**: p. 892.

79. Kim, C.-B., et al., *Rapid Photothermal Lysis of the Pathogenic Bacteria, Escherichia Coli Using Synthesis of Gold Nanorods*. Journal of Nanoscience and Nanotechnology, 2009. **9**(5): p. 2841-2845.
80. Khantamat, O., et al., *Gold nanoshell-decorated silicone surfaces for the near-infrared (NIR) photothermal destruction of the pathogenic bacterium E. faecalis*. ACS Appl Mater Interfaces, 2015. **7**(7): p. 3981-93.
81. Meeker, D.G., et al., *Synergistic Photothermal and Antibiotic Killing of Biofilm-Associated Staphylococcus aureus Using Targeted Antibiotic-Loaded Gold Nanoconstructs*. ACS Infect Dis, 2016. **2**(4): p. 241-250.
82. Huang, W.-C., P.-J. Tsai, and Y.-C. Chen, *Functional gold nanoparticles as photothermal agents for selective-killing of pathogenic bacteria*. Nanomedicine, 2007. **2**(6): p. 777-787.
83. Norman, R.S., et al., *Targeted Photothermal Lysis of the Pathogenic Bacteria, Pseudomonas aeruginosa, with Gold Nanorods*. Nano Letters, 2008. **8**(1): p. 302-306.
84. Kim, S.H., et al., *Light controllable surface coating for effective photothermal killing of bacteria*. ACS Appl Mater Interfaces, 2015. **7**(28): p. 15600-6.
85. Hsiao, C.-W., et al., *Effective Photothermal Killing of Pathogenic Bacteria by Using Spatially Tunable Colloidal Gels with Nano-Localized Heating Sources*. Advanced Functional Materials, 2015. **25**(5): p. 721-728.
86. Ju, E., et al., *Functional polypyrrole-silica composites as photothermal agents for targeted killing of bacteria*. Chem Commun (Camb), 2013. **49**(79): p. 9048-50.
87. Feng, G., et al., *Narrow band gap conjugated polyelectrolytes for photothermal killing of bacteria*. Journal of Materials Chemistry B, 2015. **3**(37): p. 7340-7346.
88. Akhavan, O., E. Ghaderi, and A. Esfandiari, *Wrapping bacteria by graphene nanosheets for isolation from environment, reactivation by sonication, and inactivation by near-infrared irradiation*. J Phys Chem B, 2011. **115**(19): p. 6279-88.
89. Jia, X., et al., *Versatile graphene-based photothermal nanocomposites for effectively capturing and killing bacteria, and for destroying bacterial biofilms*. Journal of Materials Chemistry B, 2017. **5**(13): p. 2459-2467.
90. Lin, D., et al., *Graphene oxide wrapped SERS tags: multifunctional platforms toward optical labeling, photothermal ablation of bacteria, and the monitoring of killing effect*. ACS Appl Mater Interfaces, 2014. **6**(2): p. 1320-9.

91. Turcheniuk, K., et al., *Plasmonic photothermal destruction of uropathogenic E. coli with reduced graphene oxide and core/shell nanocomposites of gold nanorods/reduced graphene oxide*. Journal of Materials Chemistry B, 2015. **3**(3): p. 375-386.
92. Kurapati, R., M. Vaidyanathan, and A.M. Raichur, *Synergistic photothermal antimicrobial therapy using graphene oxide/polymer composite layer-by-layer thin films*. RSC Advances, 2016. **6**(46): p. 39852-39860.
93. Koh, B., et al., *Fluorophore and dye-assisted dispersion of carbon nanotubes in aqueous solution*. Langmuir, 2012. **28**(32): p. 11676-86.
94. Guldi, D.M., et al., *Carbon Nanotubes in Electron Donor–Acceptor Nanocomposites*. Accounts of Chemical Research, 2005. **38**(11): p. 871-878.
95. Ballesteros, B., et al., *Single-Wall Carbon Nanotubes Bearing Covalently Linked Phthalocyanines – Photoinduced Electron Transfer*. Journal of the American Chemical Society, 2007. **129**(16): p. 5061-5068.
96. Casey, J.P., S.M. Bachilo, and R.B. Weisman, *Efficient photosensitized energy transfer and near-IR fluorescence from porphyrin–SWNT complexes*. Journal of Materials Chemistry, 2008. **18**(13).
97. Satishkumar, B.C., et al., *Reversible fluorescence quenching in carbon nanotubes for biomolecular sensing*. Nat Nanotechnol, 2007. **2**(9): p. 560-4.
98. Yang, R., et al., *Carbon Nanotube-Quenched Fluorescent Oligonucleotides: Probes that Fluoresce upon Hybridization*. Journal of the American Chemical Society, 2008. **130**(26): p. 8351-8358.
99. Yoshimura, S.H., et al., *Fluorescence labeling of carbon nanotubes and visualization of a nanotube-protein hybrid under fluorescence microscope*. Biomacromolecules, 2011. **12**(4): p. 1200-4.
100. Prakash, R., et al., *Visualization of individual carbon nanotubes with fluorescence microscopy using conventional fluorophores*. Applied Physics Letters, 2003. **83**(6): p. 1219-1221.
101. Clark, M.D., S. Subramanian, and R. Krishnamoorti, *Understanding surfactant aided aqueous dispersion of multi-walled carbon nanotubes*. J Colloid Interface Sci, 2011. **354**(1): p. 144-51.
102. Silva, W.R., E.L. Keller, and R.R. Frontiera, *Determination of resonance Raman cross-sections for use in biological SERS sensing with femtosecond stimulated Raman spectroscopy*. Anal Chem, 2014. **86**(15): p. 7782-7.

103. Berezin, M.Y., et al., *Near infrared dyes as lifetime solvatochromic probes for micropolarity measurements of biological systems*. *Biophys J*, 2007. **93**(8): p. 2892-9.
104. Qian, J., et al., *Fluorescence-surface enhanced Raman scattering co-functionalized gold nanorods as near-infrared probes for purely optical in vivo imaging*. *Biomaterials*, 2011. **32**(6): p. 1601-10.
105. Berezin, M.Y., et al., *Two-photon optical properties of near-infrared dyes at 1.55 μm excitation*. *J Phys Chem B*, 2011. **115**(39): p. 11530-5.
106. Dietze, D.R. and R.A. Mathies, *Molecular Orientation and Optical Properties of 3,3'-Diethylthiatricarbocyanine Iodide Adsorbed to Gold Surfaces: Consequences for Surface-Enhanced Resonance Raman Spectroscopy*. *The Journal of Physical Chemistry C*, 2015. **119**(18): p. 9980-9987.
107. Li, J., C. Papadopoulos, and J. Xu, *Growing Y-junction carbon nanotubes*. *Nature*, 1999. **402**: p. 253.
108. Osvath, Z., et al., *Arc-grown Y-branched carbon nanotubes observed by scanning tunneling microscopy (STM)*. *Chemical Physics Letters*, 2002. **365**(3-4): p. 338-342.
109. Ouyang, M., et al., *Atomically Resolved Single-Walled Carbon Nanotube Intramolecular Junctions*. *Science*, 2001. **291**(5501): p. 97-100.
110. Jin, C., K. Suenaga, and S. Iijima, *Plumbing carbon nanotubes*. *Nat Nanotechnol*, 2008. **3**(1): p. 17-21.
111. Luo, C., et al., *Growth mechanism of Y-junctions and related carbon nanotube junctions synthesized by Au-catalyzed chemical vapor deposition*. *Carbon*, 2008. **46**(3): p. 440-444.
112. Sano, M., et al., *Ring Closure of Carbon Nanotubes*. *Science*, 2001. **293**(5533): p. 1299.
113. Chiu, P.W., et al., *Interconnection of carbon nanotubes by chemical functionalization*. *Applied Physics Letters*, 2002. **80**(20): p. 3811-3813.
114. Weizmann, Y., D.M. Chenoweth, and T.M. Swager, *Addressable Terminally Linked DNA-CNT Nanowires*. *Journal of the American Chemical Society*, 2010. **132**(40): p. 14009-14011.
115. Palma, M., et al., *Controlled formation of carbon nanotube junctions via linker-induced assembly in aqueous solution*. *J Am Chem Soc*, 2013. **135**(23): p. 8440-3.

116. Zhu, J., et al., *Solution-Processable Carbon Nanoelectrodes for Single-Molecule Investigations*. J Am Chem Soc, 2016. **138**(9): p. 2905-8.
117. Roberts, G.S. and P. Singjai, *Joining carbon nanotubes*. Nanoscale, 2011. **3**(11): p. 4503-14.
118. Zhang, F., et al., *Structural DNA nanotechnology: state of the art and future perspective*. J Am Chem Soc, 2014. **136**(32): p. 11198-211.
119. Yang, D., et al., *DNA materials: bridging nanotechnology and biotechnology*. Acc Chem Res, 2014. **47**(6): p. 1902-11.
120. Sanchez-Pomales, G., et al., *DNA-Wrapped Carbon Nanotubes: From Synthesis to Applications*. 2010: INTECH Open Access Publisher.
121. Maune, H.T., et al., *Self-assembly of carbon nanotubes into two-dimensional geometries using DNA origami templates*. Nat Nanotechnol, 2010. **5**(1): p. 61-6.
122. Cheng, E., et al., *DNA-SWNT hybrid hydrogel*. Chemical Communications, 2011. **47**(19): p. 5545-5547.
123. Chen, Y., et al., *DNA-Directed Assembly of Single-Wall Carbon Nanotubes*. Journal of the American Chemical Society, 2007. **129**(28): p. 8696-8697.
124. Xu, P.F., et al., *DNA mediated assembly of single walled carbon nanotubes: role of DNA linkers and annealing*. Phys Chem Chem Phys, 2011. **13**(21): p. 10004-8.
125. Han, S.-p., et al., *DNA-Linker-Induced Surface Assembly of Ultra Dense Parallel Single Walled Carbon Nanotube Arrays*. Nano Letters, 2012. **12**(3): p. 1129-1135.
126. Li, S., et al., *DNA-Directed Self-Assembling of Carbon Nanotubes*. Journal of the American Chemical Society, 2005. **127**(1): p. 14-15.
127. Lu, Y., et al., *Self-assembled branched nanostructures of single-walled carbon nanotubes with DNA as linkers*. Chemical Physics Letters, 2006. **419**(4-6): p. 390-393.
128. Albertorio, F., et al., *Base dependent DNA-carbon nanotube interactions: activation enthalpies and assembly-disassembly control*. Nanotechnology, 2009. **20**(39): p. 395101.
129. Zhu, Z., et al., *Single-walled carbon nanotube as an effective quencher*. Anal Bioanal Chem, 2010. **396**(1): p. 73-83.
130. Chiu, C.F., N. Dementev, and E. Borguet, *Fluorescence quenching of dyes covalently attached to single-walled carbon nanotubes*. J Phys Chem A, 2011. **115**(34): p. 9579-84.

131. Deng, Z., et al., *The emergence of solar thermal utilization: solar-driven steam generation*. Journal of Materials Chemistry A, 2017. **5**(17): p. 7691-7709.
132. Axaopoulos, P.J. and E.D. Fylladitakis, *Performance and economic evaluation of a hybrid photovoltaic/thermal solar system for residential applications*. Energy and Buildings, 2013. **65**: p. 488-496.
133. Lewis, N.S., *Research opportunities to advance solar energy utilization*. Science, 2016. **351**(6271): p. aad1920.
134. Dincer, I. and C. Zamfirescu, *Sustainable Energy Systems and Applications*. 2011: Springer US.
135. Wang, P., *Emerging investigator series: the rise of nano-enabled photothermal materials for water evaporation and clean water production by sunlight*. Environmental Science: Nano, 2018. **5**(5): p. 1078-1089.
136. Wang, C., et al., *Synergistic effect of sunlight induced photothermal conversion and H₂O₂ release based on hybridized tungsten oxide gel for cancer inhibition*. Sci Rep, 2016. **6**: p. 35876.
137. Zhu, L., et al., *Solar-driven photothermal nanostructured materials designs and prerequisites for evaporation and catalysis applications*. Materials Horizons, 2018. **5**(3): p. 323-343.
138. Loeb, S., C. Li, and J.H. Kim, *Solar Photothermal Disinfection using Broadband-Light Absorbing Gold Nanoparticles and Carbon Black*. Environ Sci Technol, 2018. **52**(1): p. 205-213.
139. Dao, V.-D. and H.-S. Choi, *Carbon-Based Sunlight Absorbers in Solar-Driven Steam Generation Devices*. Global Challenges, 2018. **2**(2).
140. Jiang, Q., et al., *Polydopamine-filled bacterial nanocellulose as a biodegradable interfacial photothermal evaporator for highly efficient solar steam generation*. Journal of Materials Chemistry A, 2017. **5**(35): p. 18397-18402.
141. Jiang, R., et al., *Mass-Based Photothermal Comparison Among Gold Nanocrystals, PbS Nanocrystals, Organic Dyes, and Carbon Black*. The Journal of Physical Chemistry C, 2013. **117**(17): p. 8909-8915.
142. Neumann, O., et al., *Solar Vapor Generation Enabled by Nanoparticles*. ACS Nano, 2013. **7**(1): p. 42-49.
143. Neumann, O., et al., *Compact solar autoclave based on steam generation using broadband light-harvesting nanoparticles*. Proc Natl Acad Sci U S A, 2013. **110**(29): p. 11677-81.

144. Li, H., et al., *Doctor-blade deposition of quantum dots onto standard window glass for low-loss large-area luminescent solar concentrators*. *Nature Energy*, 2016. **1**(12).
145. Naumov, A.V., et al., *Analyzing Absorption Backgrounds in Single-Walled Carbon Nanotube Spectra*. *ACS Nano*, 2011. **5**(3): p. 1639-1648.